Statistical physics of nonlinear wave interaction

F. Antenucci,[1] M. Ibáñez Berganza,[2,3] and L. Leuzzi[1,2]

[1]*NANOTEC-CNR, Institute of Nanotechnology, National Research Council of Italy, Soft and Living Matter Laboratory, Rome, Piazzale Aldo Moro 2, 00185 Rome, Italy*

[2]*Dipartimento di Fisica, Università di Roma "La Sapienza," Piazzale Aldo Moro 5, I-00185 Rome, Italy*

[3]*INFN-Gruppo Collegato di Parma, viale G. P. Usberti, 7/A, 43124 Parma, Italy*

(Received 16 March 2015; published 13 July 2015)

The thermodynamic properties of vector [$O(2)$ and complex spherical] models with four-body interactions are analyzed. When defined in dense topologies, these are effective models for the nonlinear interaction of scalar fields in the presence of a stochastic noise, as has been well established for the case of the mode-locking laser formation in a closed cavity. With the help of an efficient Monte Carlo algorithm we show how, beyond the fully connected case, rich phenomenology emerges. Below a certain dilution threshold, the spherical model condenses in a nonequipartite way, while in the XY model the transition becomes continuous and the $O(2)$ symmetry remains unbroken. We attribute this fact to the invariance under gauge transformations. The introduction of topological inhomogeneities in the network of quadruplets induces some features: again symmetry conservation; the vanishing of two-point correlators; and a dynamical correlation function presenting two time scales, the large one being related to the transition between different degenerated configurations, connected by particular gauge transformations. We discuss possible experimental implications of these results in the context of nonlinear optics.

DOI: 10.1103/PhysRevB.92.014204 PACS number(s): 05.50.+q, 42.65.−k, 05.10.Ln, 11.15.Ha

I. INTRODUCTION

A. Thermodynamic approach to nonlinear optics

In the past decade there have been several fascinating attempts to understand nonlinear wave phenomena as collective, emergent behavior [1–9]. Within such a scheme, the focus is not on the kinetics of the nonlinear wave propagation [10], but on the description in terms of static quantities in a suitably defined ensemble, in such a way that different wave regimes are in correspondence with different thermodynamic phases of a Hamiltonian model.

A set of fundamental works in this context are Refs. [5–7], which describe the mechanism of passive mode-locking in multimode lasers within a statistical mechanical framework. The electromagnetic modes in this case are the longitudinal modes of the resonant cavity, and the nonlinearity is provided by a *saturable absorber*, a device which enhances high electromagnetic field intensity, hence favoring modes with large amplitude and locked phases. The temporal evolution of modes is described by a master equation [11] accounting for the nonlinear coupling of *tetrads* of modes (a four-body interaction) and with an additional stochastic drift term due to the spontaneous emission, which opposes mode locking as it tends to incoherently disorder moduli and phases. In the limit in which the dispersion can be neglected [6], the master equation leads to a Hamiltonian formulation such that the electromagnetic modes can be regarded as (complex) spin degrees of freedom, coupled by a four-body ferromagnetic interaction, while the stability of the system is assured by a global constraint on the sum of the mode intensities (a spherical constraint, in the spin language). The steady state of the laser is described by measurements in the canonical ensemble of the spin model, where the role of the temperature is played by the inverse square of *pumping rate* of the laser source. The methods of statistical physics applied to this problem reveal that, for sufficiently high ratio between the pumping rate and the noise strength, a discontinuous transition separating a para- from a ferromagnetic phase takes place [12]. In the ferromagnetic regime the phases and intensities of modes at different frequencies become *locked*, i.e., correlated, and long-range order appears, associated with $O(2)$ symmetry breaking. In the optical language this phase corresponds to a coherent light regime in which ultrashort electromagnetic pulses are generated [the *mode-locked* (ML) *regime*]. In the opposite situation, when the spontaneous emission dominates, light is in an *incoherent-wave* (IW) regime with low power efficiency and flat intensity spectrum, which is described by a paramagnetic state in the spin language. This approach allows for a treatment of the nonperturbative influence of noise and explains the discontinuous nature of the mode-locking transition, along with other properties reminiscent of discontinuous transitions as a hysteresis effect called *optical bistability* [13]. Variations of this problem have also been considered, as the active mode locking [8], injection of pulses from an external source [14], and a general agreement with experimental results has been found.

Furthermore, there have been a series of theoretical works generalizing the study of these Hamiltonians through the addition of quenched disorder in the interaction couplings [15–18]. These more complex models may represent different physical situations, such as the random laser phenomena [19], under specific assumptions [20]. In this case, a sufficiently large amount of disorder eventually leads to a glassy phase in the spin model, anticipated by a region with nonzero complexity, which is believed to describe a frustrated laser regime with the absence of long-range correlations, possibly present in random lasers.

In the relevant statistical models in this context, the electromagnetic modes are complex degrees of freedom [or $O(2)$ spins, if their amplitude dynamics can be ignored] subject to a four-body interaction which can be purely ferromagnetic or disordered. These are, in substance, XY or complex spherical p-spin ferromagnets or spin glasses, with $p = 4$. They have been studied so far in the mean-field approximation, which

is basically exact in the fully connected case. In this work we perform a systematic study of the thermodynamics of the XY and spherical models with four-body interactions beyond mean field, considering the influence of dilute topologies and of network correlations. From the optical point of view, such a generalization makes it possible to account for two ingredients of crucial importance in optical systems that could not have been considered in previous studies, in which correlations were disregarded.

First is the role of mode frequencies, $\{\omega_n\}$, which have an essential influence on the list of interacting mode tetrads since these are subject to an energy conservation prescription on their four frequencies, called the *frequency-matching condition* (see the next section). In cavity lasers it is not physically justified to neglect the influence of mode frequencies. We see that they may induce correlations in the system dynamics which lead to dramatic differences with respect to the mean-field case, and these differences have clear physical consequences in the optical counterpart.

Second is the presence of dilution in the interaction network, from the fully connected down to the sparse network with an extensive number of tetrads. This element is necessary, e.g., to account for the onset of lasing in more complicated experimental setups as the random laser, in which the interaction sparseness depends on the spatial superposition of the electromagnetic fields of the modes. As we will see, a sufficiently large degree of dilution induces nontrivial changes in the nature of the XY transition. Furthermore, in the spherical model case, the dilution induces a transition to a regime in which the nonlinearity prevents the equipartition of energy. Since the seminal work of Fermi, Pasta, and Ulam [21], the nonequipartition of energy induced by nonlinearity is one of the crucial phenomena in nonlinear physics that claims for a statistical treatment [1,3].

From the point of view of statistical mechanics, the models investigated in this article present a remarkably rich phenomenology when fluctuations are allowed to take place. As we explain in Sec. I C, the Ising model with $p = 4$ has already been considered beyond mean-field approximation, exhibiting slow dynamics and other kinetic features characteristic of glass formers. The XY model with suitable lattice plaquette interactions is an effective lattice model for the gauge $O(2)$ field theory describing electromagnetism. However, this work considers the four-body XY model within a statistical mechanical framework, beyond mean-field approximation.

We show how in the arena of these models one can find, according to the dilution and the presence or absence of topological correlations, a variety of phenomenology ranging from the symmetry conservation (reminiscent of the Kosterlitz-Thouless transition) to different orders of the transition, nonequipartite energy localization, and slow dynamics, among other features.

To better motivate the study of these models in the optical context, we review in some detail the Hamiltonian approach to the passive mode-locking transition in the next section. In Sec. I C we review precedent studies of four-body interactions in statistical physics. We then define the models under study and describe their properties in Sec. II. The effect of a sufficiently large amount of dilution on them is described in Sec. III. Section IV is dedicated to the numerical methods that we have employed, and the consequent results about the spherical and XY models are exposed in Secs. V and VI, respectively. We then draw some analogies between these results and similar phenomena occurring in lattice gauge theories (Sec. VII) and propose possible physical consequences in the field of nonlinear optics in Sec. VIII. Our conclusions are in Sec. IX.

B. Statistical approach to mode locking

The evolution of the electromagnetic mode $a_l \in \mathbb{C}$ in a standard passive mode-locking laser is expressed through the well-known master equation [11]

$$\frac{d}{dt}a_l(t) = (G_l + \imath D_l)a_l(t) + (\Gamma - \imath\Delta) \times {\sum_{k_1,k_2,k_3}}' a_{k_1}(t)a^*_{k_2}(t)a_{k_3}(t) + F_l(t); \tag{1}$$

here the parameter G_l represents the difference between the gain and loss of the mode l in a complete round-trip through the cavity, D_l is the group velocity dispersion of the wave packet, Γ is the nonlinear self-amplitude modulation coefficient associated with a saturable absorber and, hence, to the passive mode locking, and Δ is the self-phase modulation coefficient (responsible for the Kerr lens effect). The noise $F_l(t)$ is generally assumed Gaussian, white, and uncorrelated,

$$\begin{aligned} \langle F^*_{k_1}(t_1)F_{k_2}(t_2)\rangle &= 2T_0\delta_{k_1k_2}\delta(t_1 - t_2), \\ \langle F_{k_1}(t_1)F_{k_2}(t_2)\rangle &= 0, \end{aligned} \tag{2}$$

where T_0 is the spectral power of the noise.

A fundamental element, which deserves particular attention in this paper, is that the sum in the nonlinear term in Eq. (1) is restricted to the tetrads of modes such that the *frequency-matching condition* (FMC),

$$|\omega_l - \omega_{k_2} + \omega_{k_3} - \omega_{k_4}| \lesssim \gamma, \tag{3}$$

is satisfied, where γ is the single-mode linewidth.

In the following we are interested in the purely dissipative case, in which the group velocity dispersion and the Kerr effect can be neglected. This includes the important case of soliton lasers [6]. The purely dissipative situation plays an exceptional role in our approach: In this case, the evolution depicted by Eq. (1) is Hamiltonian, while the system remains stable because the gain decreases as the optical intensity increases [22]. To study the equilibrium properties of the model, this last element can be included, considering an equivalent variant of the model where the gain assumes the value that exactly keeps the total *optical power*, $\mathcal{E} = \sum_j |a_j|^2$, constant of motion, as Gordon and Fischer proposed in Ref. [5]. In this way the system evolves over the hypersphere:

$$\sum_j |a_j|^2 \equiv \epsilon N. \tag{4}$$

In this situation, the effective temperature in the statistical model is inversely proportional to the squared optical power, $T \equiv T_0/\epsilon^2$, where T_0 is the true heat-bath temperature. Equivalently, the parameter that drives the transition in the photonic system can be expressed through the so-called *pumping rate*, $\mathcal{P}^2 = T^{-1}$.

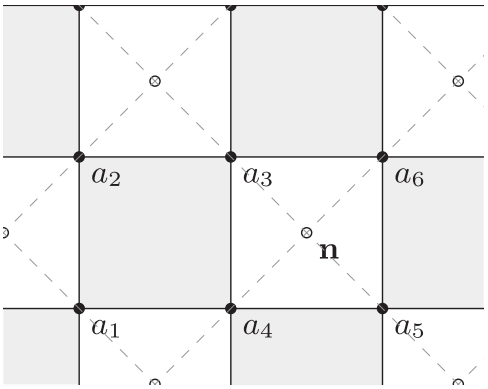

FIG. 1. Illustration of the disposition of the interacting quadruplets in a lattice gauge model in $d = 2$ dimensions. The sets of four indices $(ijkm)$ contributing to the energy (by a quantity $-\mathrm{Re}[a_i a_j^* a_k a_m^*]$) is given by the gray lattice plaquettes. The so-defined Hamiltonian is invariant under transformations consisting of rotating by a phase the degrees of freedom of the white plaquettes (associated to given sites of an auxiliary lattice, represented with dashed lines). If one associates a phase $\varphi_{\mathbf{n}} \in [0,2\pi)$ to the plaquette defined by the auxiliary lattice site $\mathbf{n}$, the transformation is $a_i \to a_i e^{\imath\varphi_{\mathbf{n}}}$ for $i = 3,4,5,6$. An equivalent construction is done for $d > 2$ lattices [23].

C. Previous studies of four-body models: Lattice gauge theories

Ising models with four-body (lattice plaquette) interactions have been studied as cutoff regularized versions of scalar gauge theories [23]. If the interacting quadruplets are suitably defined in terms of plaquettes of a hypercubic lattice in d dimensions, the model energy becomes invariant under flipping sets of four neighboring spins (see Fig. 1 for details). The $p = 4$ Ising model so defined is called *Ising lattice gauge theory* and is known to present a single, disordered phase for any nonzero temperature in $d = 2$, when it is equivalent to an independent set of $d = 1$ pairwise Ising models. In $d = 3$ the Ising lattice gauge theory exhibits a phase transition, which is related to the $d = 3$ Ising model transition. The low-temperature phase is, however, unmagnetized, as a consequence of the local gauge symmetry: the expectation value of any operator not invariant under local gauge symmetries vanishes, a result called Elitzur's theorem [23]. The magnetization is a one-body observable, not invariant under the 4-spin flipping gauge transformation, and it consequently vanishes. The nature of the low-temperature phase is unveiled instead by the gauge-invariant correlation function, or the expectation value of bunches of spins whose positions draw a planar close contour in the lattice. Such a nonlocal operator is helpful to interpret the phase transition as a confinement-deconfinement condensation of kinks, rather than a usual order-disorder transition found in pairwise models. In a different context, classical Ising models with four-body interactions are also studied as effective models for the interaction of superconducting electrons or grains [24,25].

$p = 4$ Ising models have also been studied from a statistical physical point of view [26–32]. They are, in particular, subject of interest as far as their plaquette version may exhibit slow dynamics and other dynamical features reminiscent to those of glasses, which are self-induced (i.e., not induced by quenched disordered couplings) [28–31]. The system with interacting quadruplets defined as the plaquettes of a hypercubic lattice (the *plaquette Ising model*) has been particularly studied. In two dimensions it presents a phase transition with dynamical activated behavior [33]. In three dimensions the model is called the Gonihedric model [34,35] and is known to exhibit a first-order phase transition and a degenerated ground state [26,28,36]. The slow dynamics, metastability and glasslike features of the 3D model have been studied in Refs. [28,31,37,38]. An anisotropic variant of the Gonihedric model has been recently studied [39], its dynamical properties are shown to be signaled by the expectation values of quantum information-theoretical estimates in its quantum counterpart.

The $O(2)$ generalization of the lattice gauge-invariant model, called Abelian gauge theory, presents a larger, $O(2)$, local gauge invariance. Indeed, its behavior at low temperature is described in the continuum limit with the Euclidean action of electrodynamics, according to a spin-wave approximation resembling the one that makes it possible to describe the undercritical temperature of the $d = 2$ $O(2)$ model in terms of a Gaussian theory [23]. As in the Ising gauge theory, the $d = 2$ Abelian gauge theory presents no phase transition, while the $d = 3$ presents a phase transition separating two unmagnetized phases and, again, the order parameter being a nonlocal contour correlator, an object which is directly related with the potential energy of deconfinement, in the field theoretical language.

II. THE LEADING MODELS: $p = 4$ XY AND COMPLEX SPHERICAL MODELS

A. Definition of the model

We are interested in the statistical analysis of the mode wave interaction Hamiltonian, introduced in Sec. I B. We restrict our analysis to the four-body interaction term, as it contains the essential nonlinear phenomenology. The inclusion of the local interaction due to a nonflat gain [see Eq. (1)] does not change the thermodynamic features of the model, and its inclusion is discussed in Sec. VIII C.

We, then, consider a set of N electromagnetic modes whose amplitudes are described by the complex numbers a_m, $m = 1,\ldots,N$, with phases $\phi_m = \arg a_m$ and moduli $A_m = |a_m|$. The Hamiltonian, $\mathcal{H}$, is completely specified in this case by the list of *quadruplets*, or *ordered* sets of four mode indices $(spqr)$, which correspond to different terms in $\mathcal{H}$. The list of quadruplets can be specified by the *adjacency tensor*, $\mathcal{A}_{sprq}$, equal to 1 whenever the quadruplet defined by its indices is a term of the Hamiltonian, and zero otherwise. Hence, $\mathcal{H}$ takes the form [5] [see Eq. (1)]

$$\mathcal{H} = -\frac{J_0}{8} \sum_{s,p,q,r} \mathcal{A}_{spqr} A_s A_p A_q A_r \times \cos(\phi_s - \phi_p + \phi_q - \phi_r), \tag{5}$$

while the mode amplitudes are constraint by Eq. (4). This model corresponds to the (ferromagnetic) four-body complex spherical model (CSM) in an arbitrary topology of quadruplets. In the particular case where the moduli A_m are *fixed* and all equal to 1, the Hamiltonian reduces to the four-body XY

$[O(2)]$ model:

$$\mathcal{H}_{XY} = -\frac{J_0}{8} \sum_{s,p,q,r} \mathcal{A}_{spqr} \cos(\phi_s - \phi_p + \phi_q - \phi_r). \quad (6)$$

B. Symmetry of the list of quadruplets

The adjacency tensor $\mathcal{A}$ is, in general, not symmetric under permutations of its indices. However, it exhibits a symmetry which is also in each one of the terms in the Hamiltonian (5). Given an *ordered* set of four indices, its 24 possible permutations (i.e., quadruplets) can be split into three nonequivalent subsets of the 8 permutations that have the same energy. Moreover, if a quadruplet respects the FMC, then all of its 8 equivalent permutations do. The three nonequivalent permutations can be chosen to be $\mathcal{Q} = \{(1234),(1324),(4231)\}$, in such a way that the Hamiltonian can be then written as

$$\mathcal{H} = -J_0 \sum_{s<p<q<r} \sum_{\pi \in \mathcal{Q}} \mathcal{A}_{\pi_s \pi_p \pi_q \pi_r} A_{\pi_s} A_{\pi_p} A_{\pi_q} A_{\pi_r} \times \cos\left(\phi_{\pi_s} - \phi_{\pi_p} + \phi_{\pi_q} - \phi_{\pi_r}\right), \quad (7)$$

where π_s are the members of the permutation, $\pi = (\pi_1 \pi_2 \pi_3 \pi_4)$. This is the origin of the $1/8$ factor in Eq. (5). The size scaling of J_0 is to be fixed in such a way that the energy $E = \langle H \rangle$ is an extensive quantity in both low- and high-temperature phases. We treat this point in Sec. III.

C. Topology of quadruplets

In the following analysis we have considered two types of topologies $\mathcal{A}$.

1. Homogeneous topology (HT)

The quadruplets are selected uniformly at random. The desired number of quadruplets (or ordered sets of four indices), N_4, are randomly chosen among all the possible quadruplets. Specifically, in order to preserve the permutation symmetry of the Hamiltonian (cf. Sec. II B), this random selection is performed by randomly selecting $N_4/8$ quadruplets among all possible $N(N-1)(N-2)(N-3)/8$ quadruplets with different energy, and, for each one, we append all their eight equivalent permutations to the list. We call *fully connected* the particular case of the HT such that all quadruplets are considered.

We stress that in the HT case, hence, the list of quadruplets is not conditioned by the set of frequencies. In the photonic language, this situation corresponds to the case of the so-called *narrow frequency distribution*, in which the different frequencies ω_n are all similar in magnitude, the difference between them being lower than the linewidth γ, so that the FMC [Eq. (3)] is trivially satisfied.

2. Correlated topology (CT)

The quadruplets are no longer chosen in an uncorrelated way, although they are still stochastically chosen. We randomly select $N_4/8$ quadruplets with different energy, *only* among the possible $\sim N^3$ quadruplets $spqr$ satisfying the relation

$$s - p + q - r = 0, \quad (8)$$

and, for each one, we append all its eight equivalent permutations to the list. This prescription is the result of imposing a FMC [cf. Eq. (3)] if one supposes a set of N frequencies distributed as a linear comb,

$$\omega_m = \omega_0 + m\,\delta\omega, \quad \delta\omega \gg \gamma, \quad (9)$$

which is the case of interest describing closed cavity lasers. The FMC identity has become an integer identity since, in the optical interpretation, the values ω_m are to be understood as the centers of the bins of a discrete frequency distribution whose bin width is given by the linewidth γ, so that Eq. (3) becomes equivalent to Eq. (8).

Besides having a clear physical motivation (the equispaced frequency case), the constraint Eq. (8) is also the simpler and most natural way of introducing correlations in an abstract stochastic set of interacting quadruplets. Consider the analogy with a random network: A way to construct random but correlated graphs is by introducing some kind of distance between different nodes (as the absolute value of the difference between the node indices $d_{sp} = |s - p|$) and choosing bonds with a probability depending on such a distance. In the case of the list of quadruplets, one needs a four-index function, and a similar role can be played by $d_{spqr} = |s - p + q - r|$. The FMC with the equispaced set of frequencies is equivalent to choosing quadruplets presenting the minimum value, $d_{spqr} = 0$. In this way, the mode frequencies are not a degree of freedom, but a coordinate driving correlations as distance in a graph. This resembles the Golay-Bernasconi model [40,41], where instead one is interested to find the sequences with low autocorrelation.

While there is a stochasticity in both homogeneous and CT, due to the fact that only a random fraction of the possible quadruplets are considered, there is an important difference: In the HT, the average number of quadruplets connecting two nodes is independent of the nodes in the quadruplet, while in the CT one can show that the number of quadruplets (normalized as a probability distribution) connecting couples of nodes with frequency difference $\omega_i - \omega_j$, i.e., at a distance $|i - j|$, is $h(x) = 2(-x + 1)$, where $x = |i - j|/N$. Modes with similar frequencies are connected by a higher number of quadruplets (and, consequently, effectively more coupled) in Eq. (5). This difference is illustrated in Fig. 2: We show the difference through the *from-quadruplet graph*, or a weighted graph such that each node represents a mode, and the edge weight (represented by the line thickness) is proportional to the number of quadruplets containing their modes.

There are good reasons to classify the interaction topology in the two types, HT, CT. As we explain below, if $N_4 \sim \mathcal{O}(N^{\geq 2})$, the thermodynamic behavior of the system is completely determined by the type of topology of quadruplets and not by N_4, and it is essentially different in the HT and CT cases. The frequency correlations in the last case induce correlations between mode amplitudes with different frequencies, $a_j a_{j'}$, that will drastically modify the thermodynamic phases, as shown in Sec. V.

One may ask why we study stochastic sets of quadruplets instead of considering, for example, deterministic sets given by the four nodes composing a plaquette of a d-dimensional hypercubic lattice, as done for the Gonihedric model in the works mentioned in the Introduction. The answer is given, on

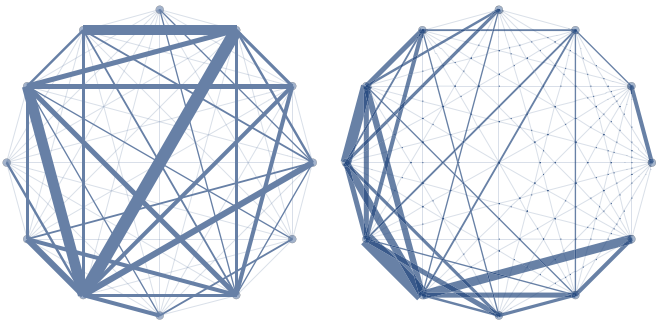

FIG. 2. (Color online) From-quadruplet graphs of two lists of quadruplets with $N = 12$, $N_4 = 97$ and homogeneous (left) and correlated (right) topology, respectively. Adjacent nodes represent adjacent mode indices, and the thickness of a link is proportional to the number of quadruplets that contain the two linked nodes. The angular position of a node corresponds to its index, so that nodes on adjacent clock hours have adjacent frequencies. The central frequencies are at 9 and 10 o'clock. For the HT the thickness is uncorrelated to the position. For the CT it is apparent that the thickest links are between adjacent modes. Moreover, in the CT case the modes at the center of the spectrum (at 9 and 10 o'clock) share more quadruplets than those at the edge (at 3 and 4 o'clock).

the one hand, by the fact that the $p = 4$ ferromagnetic spherical model, as we explain in the next section, presents a trivial thermodynamic behavior when the number of quadruplets is low enough and, in particular, in the $N_4 \sim \mathcal{O}(N)$ case corresponding to the plaquette-based list of quadruplets. From the point of view of optics, on the other hand, the present system is relevant for the description of a closed cavity laser, such that, in principle, each mode interacts with the rest of the modes (the fully connected case). This would lead to $N_4 \sim \mathcal{O}(N^4)$ [or to $N_4 \sim \mathcal{O}(N^3)$ with the constraint Eq. (8)], a situation which is incompatible with the plaquette-based topology. Finally, we stress that there is a convenience for studying stochastic sets of quadruplets: Such dilute systems can be numerically processed more efficiently, hence the usefulness of the dilute ensemble of quadruplets. This point is discussed in Sec. IV.

III. ROLE OF THE QUADRUPLET DILUTION THRESHOLD

A. Nonequipartite condensation in the complex spherical model

As will see, the complex spherical model presents a trivial low-temperature behavior, that we call *nonequipartite condensation*, whenever the number of quadruplets is low enough, $N_4 \sim \mathcal{O}(N^{<2})$ for the ferromagnetic case. The nonequipartite condensation is such that all the spherical constraint Eq. (4) is concentrated in a low, $\mathcal{O}(1)$ number of sites, whose amplitudes are $A \sim \mathcal{O}(\sqrt{N})$. In this case, the energy in the low-temperature phase is of order $E \sim -J_0 N^2$. The *equipartition*, alternative to the nonequipartite condensation, is characterized by a $A \sim \mathcal{O}(1)$ in both phases; hence, $E \sim -J_0 N_4$. In the latter case, the low-T phase is characterized by the homogeneity of spin moduli, which tend to *lock*, i.e., to become equal throughout the system, contrarily to the former case. One observes that the energy is lower (of a larger order with N) in the nonequipartite condensation whenever $N_4 \sim \mathcal{O}(N^{<2})$. Requiring the extensivity of the energy one obtains that, according to the type of condensation, J_0 is subject to satisfy the following scaling

$$J_0 \sim \begin{cases} 1/N & \text{nonequipartition} \quad [N_4 \sim \mathcal{O}(N^{<2})], \\ N/N_4 & \text{equipartition} \quad [N_4 \sim \mathcal{O}(N^{>2})]. \end{cases} \tag{10}$$

For high-enough temperature, one expects a disordered phase with uncorrelated and equipartited spins. The extensivity of the energy requires $J_0 N_4 \sim \mathcal{O}(N)$, implying in its turn that the nonequipartite condensation does not occur for $N_4 \sim \mathcal{O}(N^{>2})$, confirming Eq. (10).

This argument does not apply to the marginal situation $N_4 \sim \mathcal{O}(N^2)$. We expect, however, equipartition, since in this circumstance there is an extensive entropic contribution to the free energy. This is in agreement with our numerical results for all the considered systems satisfying $N_4 \sim \mathcal{O}(N^2)$, which turn out to be equipartite.

In the following we are interested in the equipartite case. We, hence, consider from now on systems with $N_4 \sim \mathcal{O}(N^{\geqslant 2})$. Our Hamiltonian, in its final form, will be taken as [see Eq. (10)]

$$\mathcal{H} = -\frac{N}{8N_4} \sum_{spqr} \mathcal{A}_{spqr} A_s A_p A_q A_r \times \cos(\phi_s - \phi_p + \phi_q - \phi_r). \tag{11}$$

B. Nonequipartition in the disordered complex spherical model

Although in the next section our numerical analysis focuses on the ferromagnetic case, for completeness we also discuss how the nonequipartite condensation occurs in the quenched disordered case below the higher threshold $N_4 \sim \mathcal{O}(N^3)$. The argument is based on a mean-field approximation making it possible to compute the scaling of the average energy with N, N_4 within the replica formalism. The details can be found in Appendix B. Supposing that the coupling J in Eq. (5) is no longer ferromagnetic but Gaussian distributed with average J_0 and variance σ, one has that the energy scaling in both nonequipartite and equipartite types of condensation goes as

$$E \sim \begin{cases} \text{nonequipartite} & -(J_0 + \sigma)N^2, \\ \text{equipartite} & -(J_0 + \sigma^2)N^2, \end{cases} \tag{12}$$

so that for the extensivity of the energy one is forced to take for σ the minimum between N/N_4 and $1/N^2$. Hence, the threshold between nonequipartition and equipartition becomes, in this case, $N_4 = \mathcal{O}(N^3)$. This threshold is compatible with the provisional results of our simulations in the presence of disorder (which will be reported in a future communication).

C. Magnetized-to-unmagnetized threshold of the XY model for low number of quadruplets

An equivalent threshold effect is observed for the $p = 4$ XY ferromagnet [Eq. (6)], with HT. In this case the threshold is, instead, the extensive situation $N_4 \sim \mathcal{O}(N)$, above which the system presents a low-temperature phase with spontaneous breaking of the $O(2)$ symmetry. Below and at the threshold, i.e., for $N_4 \sim \mathcal{O}(N^{\leqslant 1})$, the model remains unmagnetized. This fact is discussed in more detail in Sec. VI.

IV. NUMERICAL ANALYSIS

A. Efficient Monte Carlo simulation: The synchronous Monte Carlo algorithm

We have performed a Monte Carlo (MC) integration using a homemade algorithm dealing with vector $p = 4$ interaction models in arbitrary topologies. The algorithm uses local updates (in the spherical model case it is not possible to use cluster updating, due to the nonlocality induced by the spherical constraint). The parallel tempering algorithm has been used to enhance equilibration in large systems.

Moreover, for most of the results presented in this article we have used a parallel, high-performing version of the algorithm, running on graphics processing units. The parallel Monte Carlo sampling of a system of interacting spins requires the division of the set of spins in noninteracting subsets, such that the members of each one can be processed in parallel. In bipartite lattices, such a division is called the checkerboard decomposition, while, in general, graphs defining the pairwise interaction require the *coloring* of the graph in such a way that all spins with identical color are processed in parallel and different colors are processed sequentially [42]. As explained before, the case of interest is a system in which the topology of the interaction is given by a set of at least $\mathcal{O}(N^2)$ quadruplets between N modes, so that each mode possesses an extensive number of *quadruplet neighbors*, i.e., of modes such that there is at least a quadruplet connecting both. As a consequence, the MC parallelization of such a highly connected system is, in principle, unfeasible.

However, parallel MC techniques can still be used in this case. We have observed that, quite remarkably, there are circumstances (that will be specified elsewhere) in which applying the so-called *synchronous MC* rule (i.e., to all spins in parallel, regardless of their connectivity), one recovers the correct results. Although one is making an error in each update (since one updates interacting spins simultaneously), the overall error averages down to zero. In a fully connected $p = 2$ spin model the fully parallel MC update does not differ with respect to a sequential MC scheme, as it has been already observed [43]. In the present case with $p =$ 4-body interactions and $\mathcal{O}(N^{\geqslant 2})$ quadruplets, the results of the synchronous MC are, again, consistent with the serial algorithm.

It is particularly remarkable that for the present model it is not necessary to have a fully connected system for the synchronous MC algorithm to work: a dilute, but connected-enough system is sufficient to obtain results which are indistinguishable from that of the serial MC algorithm. Interestingly, this holds true even if the transition is no longer describable in mean-field approximation: We show that in the CT case fluctuations arise and change the nature of the transition and, even in this case, the synchronous MC leads to correct results.

An example of the reliability of the synchronous MC is shown in Fig. 3 for the average energy in the HT, but the picture is valid also for the CT case. The measures are always compatible for a serial MC and a parallel MC. In the low-temperature phase, in particular, the values are numerically indistinguishable. Some appreciable deviations are observed only in the high-temperature phase in the case of diluted systems ($N_4 = N^2$ in Fig. 3). In this case the synchronous algorithm predicts an average energy which is closer to zero, although compatible with the serial algorithm within thermal fluctuations. For $T > T_c$, the synchronous algorithm has hence the effect of masking finite-size effects, since the energy per site E/N vanishes at large N for $T > T_c$.

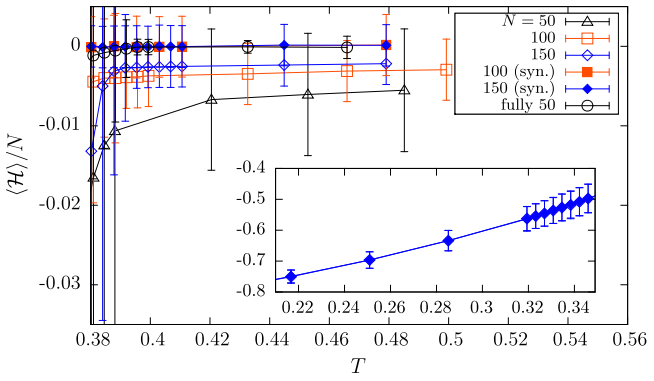

FIG. 3. (Color online) High-temperature intensive energy versus temperature for systems with three sizes in a diluted HT with $N_4 = N^2$ quadruplets, computed with the serial MC algorithm (open symbols for $N = 50, 100, 150$). The results obtained with the synchronous update for these systems (corresponding full symbols for $N = 100, 150$) yield an average value closer to zero, though compatible in the statistical uncertainty. At low temperature both algorithms accurately coincide and the results are indistinguishable, as displayed in the inset for $N = 150$. Note that the fully connected system (open circles), simulated by means of a serial MC, exhibits a zero energy at high T yet for $N = 50$.

B. Observables of interest

Besides the energy, $E = \langle\mathcal{H}\rangle$, we consider the following observables. First is the specific heat:

$$c = \frac{1}{N}\frac{\partial\langle\mathcal{H}\rangle}{\partial T} = \frac{\langle\mathcal{H}^2\rangle - \langle\mathcal{H}\rangle^2}{N\,T^2}. \tag{13}$$

Also, the *average modulus,* $\langle r\rangle$, with r being

$$r = \frac{1}{N}\sum_j A_j, \tag{14}$$

a quantity which is related with the site fluctuations of the modulus: $\frac{1}{N}\sum_j (|a_j| - r)^2 = 1 - r^2$. The larger is r, the more *locked* are the moduli of the spins in a given configuration, and $r = 1$ corresponds to a configuration with all the mode amplitudes that have modulus equal to 1. Another interesting observable is the *magnetization*, $\langle m\rangle$, where m is the complex number,

$$m = \frac{1}{N}\sum_j a_j, \tag{15}$$

along with its Cartesian components, $m_x = \mathrm{Re}[m]$ and $m_y = \mathrm{Im}[m]$.

Finally, we also measure *frequency correlation functions*, which are ensemble averaged correlations between modes whose frequencies differ by a given quantity, ω. These observables acquire full sense in the CT case, when the mode frequencies play a role in the topology and, hence, in

the thermodynamics. We define, in particular, the *intensity correlation function*, $C_{\rm i}$,

$$C_{\rm i}(\omega) = \frac{1}{K(\omega)} \left\langle \sum_{i,j=1}^{N} A_i^2 A_j^2 \, \delta(\omega_i - \omega_j + \omega) \right\rangle, \tag{16}$$

$K(\omega) = \sum_i \sum_j \delta(\omega_i - \omega_j + \omega)$ being the normalization, along with the *phase correlation function*, $C_{\rm p}$,

$$C_{\rm p}(\omega) = \frac{1}{K(\omega)} \left\langle \sum_{i,j=1}^{N} \cos(\phi_i - \phi_j) \, \delta(\omega_i - \omega_j + \omega) \right\rangle. \tag{17}$$

We also define their respective *connected* functions,

$$\bar{C}_{\rm i}(\omega) = C_{\rm i}(\omega) - \frac{1}{K(\omega)} \sum_{i,j=1}^{N} \left\langle A_i^2 \right\rangle \left\langle A_j^2 \right\rangle \delta(\omega_i - \omega_j + \omega), \tag{18}$$

and idem for $\bar{C}_{\rm p}(\omega)$.

C. Details of the simulations

We have considered finite-size realizations for several values of N, ranging from $N = 50$ to $N = 10^3$, depending on the topology and N_4. As an equilibration test we have verified the stationarity of the distributions of observables in different MC time windows of exponentially increasing length and the symmetry of the histograms of the single components of the magnetization, $h(m_{x,y}) = h(-m_{x,y})$ (cf. Fig. 11).

Throughout our analysis, we have not performed systematic averages over realizations of the list of quadruplets in none of the topology types (HT, CT). This is justified since the fluctuations of thermodynamic quantities among different realizations of the interaction network are at least one order of magnitude less than thermal fluctuations. In Fig. 4 we show how thermal fluctuations are larger than topological fluctuations of the energy in the worst case analyzed: the $N = 50$ with $N_4 \sim \mathcal{O}(N^2)$ quadruplets distributed with the CT (i.e., the smallest, most inhomogeneous system).

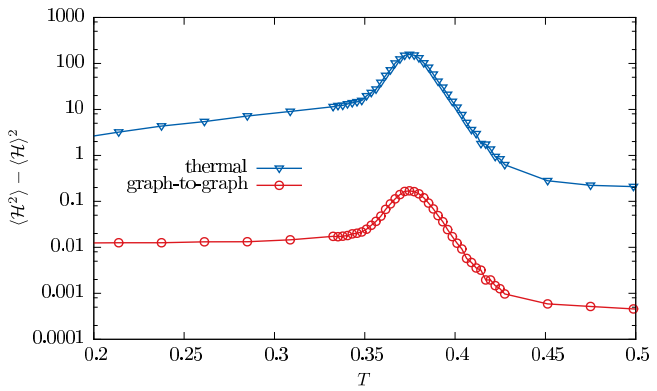

FIG. 4. (Color online) Thermal energy fluctuations versus topological (graph-to-graph) fluctuations of a CT system with $N = 50$ and with $N_4 = N^2$ quadruplets. The topological fluctuations have been computed over a set of 100 realizations of the list of quadruplets.

V. NUMERICAL RESULTS FOR THE COMPLEX SPHERICAL MODEL

We now present the results of our MC analysis for the complex spherical model. The most salient feature of our simulations is the presence of a phase transition of first-order nature. The phase transition separates a high-T phase with randomly distributed degrees of freedom, zero magnetization, and zero energy per mode for large N from a low-temperature phase with *(1) locked moduli and phases(2)* nonzero spin-spin correlations, at least in single configurations and for moderate time scales.

A remarkable observation is the irrelevance of random dilution: For both kinds of topologies the results of our simulations are independent of the number of quadruplets, as far as this quantity is above the threshold $N_4 \sim \mathcal{O}(N^{\geqslant 2})$, corresponding to equipartite systems. This means that the results (with the only exception of the finite-size scaling of the critical temperature) remain unchanged in the broad range of N_4 scaling from $\sim N^4$ down to $\sim N^2$.

There is an essential difference between the thermodynamic behavior of the system in the presence of homogeneous and correlated topologies: In the first case the behavior is compatible with the mean-field solution, the low-temperature phase is spontaneously magnetized, and spin-spin correlators are nonzero. In contrast, for CTs the results significantly differ from the mean-field solution; there is lack of spontaneous magnetization at low temperatures, and two-point correlators turn out to vanish.

As already mentioned, we have found phase transitions of different nature (first and second order), and different low-temperature states (magnetized and unmagnetized, with zero and nonzero two-point correlators), depending on the kind of topology, the dilution, and the model (XY/CSM). Before describing in detail our results, we anticipate that these general features are outlined in Table I.

A. Homogeneous topology

General features and comparison with mean-field theory

We first consider the HT system and the fully connected case (i.e., with all the possible quadruplets active) as a particular case of it. Our first, already-mentioned, result is that, given the topology type, the dilution turns out to be

TABLE I. Nature of the transitions and of the correlators in the low-T phase for the different considered models, as emerges from the numerical analysis. Whenever $\langle m \rangle = 0$, also the two-point correlators $\bar{C}_{\rm i,p}$ vanish.

Model	Topology	N_4	Transition	$\langle m \rangle (T < T_c)$
CSM	HT	$\mathcal{O}(N^{\geqslant 2})$	First-order	$\neq 0$
CSM	HT	$\mathcal{O}(N^{<2})$	non-Eq. cond.	
CSM	CT	$\mathcal{O}(N^{\geqslant 2})$	First-order	$= 0$
CSM	CT	$\mathcal{O}(N^{<2})$	non-Eq. cond.	
XY	HT	$\mathcal{O}(N^{>1})$	First-order	$\neq 0$
XY	HT	$\mathcal{O}(N)$	Second-order	$= 0$
XY	CT	$\mathcal{O}(N^{>1})$	First-order	$= 0$
XY	CT	$\mathcal{O}(N)$	First-order	$= 0$

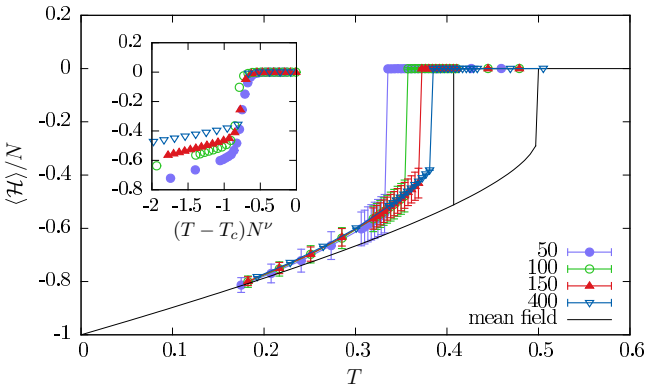

FIG. 5. (Color online) Energy per spin versus temperature for several sizes in the HT with $N_4 = N^2$. The finite-size critical temperature $T_c(N)$ increases with size. The inset shows that the data (with the same symbol meaning of the main figure) satisfies a scaling of the form $T_c(N) - T_c^{\rm mf} \sim N^{-b}$, with $b = 0.6$, indicating that they are compatible with the mean-field critical temperature for large N. The two vertical lines of the mean-field curve are in correspondence to the transition and to the spinodal temperature.

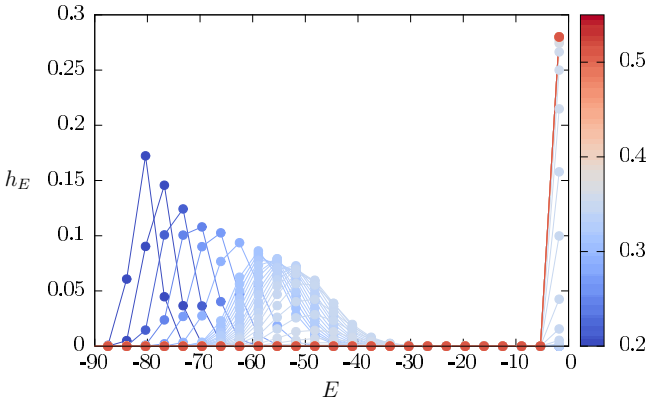

FIG. 6. (Color online) Histogram of the energy at several temperatures of a $N = 100$ system in the HT with $N_4 = N^2$. There is a temperature range in which the high-T and the low-T peaks coexist.

irrelevant: The intensive quantities for values of N_4 lower than its maximum value are indistinguishable, within statistical errors, from that of the fully connected case. We thus expect the behavior in the HT to coincide in the large-N limit with the mean-field solution of the model [5,18]; cf. Appendix A. This predicts for the transition temperature $T_c^{\rm mf} = 0.407\,26$. In Fig. 5 we present a finite-size analysis of the energy E in the case of a homogeneous set of $N_4 \sim \mathcal{O}(N^2)$ quadruplets. The high-temperature phase has zero energy and decreases discontinuously at a size-dependent value $T_c(N)$. As shown in the figure inset for the $N_4 \sim \mathcal{O}(N^2)$ case, the finite-size scaling of the transition temperature, $T_c(N) = kN^{-b} + T_c(\infty)$, leads to an infinite-volume $T_c(\infty)$, which is compatible with $T_c^{\rm mf}$, for all the studied sets of quadruplets [44].

In Fig. 5 we also present the energy as a function of temperature for the marginal mean-field solution shown in Appendix A,

$$E_{\rm mf}(T) = -\frac{1}{4}[1 + (1 - 2T)^{1/2}]^2, \quad T < T_c. \qquad (19)$$

It is apparent how, while the value of the critical temperature estimated by finite-size scaling on simulation data coincides with the mean-field analytical solution, the behavior of $E_{\rm mf}(T)$ below the transition does not coincide with the numerics. This difference decreases with decreasing temperature, eventually vanishing at zero temperature. Such a discrepancy is absent in both the XY and the real spherical model, for which the respective mean-field solutions exactly describe the behavior of finite-size systems already at quite small sizes at all temperatures, as we have verified numerically.

In the ordered phase, there may be a correlation between the angle fluctuations of a site, i, and the value of its radius, r_i. We expect such a correlation since smaller radii contribute less to the energy and, consequently, their angle fluctuations are higher. We suggest that these angular fluctuations are underestimated in the mean-field description (which does not account for site-to-site fluctuations) and are responsible for the discrepancy described above. This argument justifies the fact that the difference between mean-field theory and the numerical data increases with T, that the numerical energy is underestimated, and that there is no such a discrepancy in the spherical and XY models, in which there is only one degree of freedom. In any case, the mean-field derivation in Appendix A is supposed to describe exactly the fully connected system in the large-N limit: There is need of further investigation to clarify this unexpected behavior.

The finite-size transition temperatures $T_c(N)$ reported as vertical lines in Fig. 5 have been calculated from the bimodal energy probability distribution (cf., Fig. 6) because the temperatures at which the high- and low-energy peaks enclose equal areas. We have also considered the metastable continuation of the disordered phase energy, averaging over the disordered peak only, and a temperature limit of the metastable regime (a *spinodal temperature*, T_s) as the one at which the low-energy peak vanishes. As shown in Fig. 7, the quantity $T_s(N) - T_c(N)$ decreases with increasing size, thus indicating that again the metastability behavior of the model is different from that predicted by the marginally stable mean-field solution, which

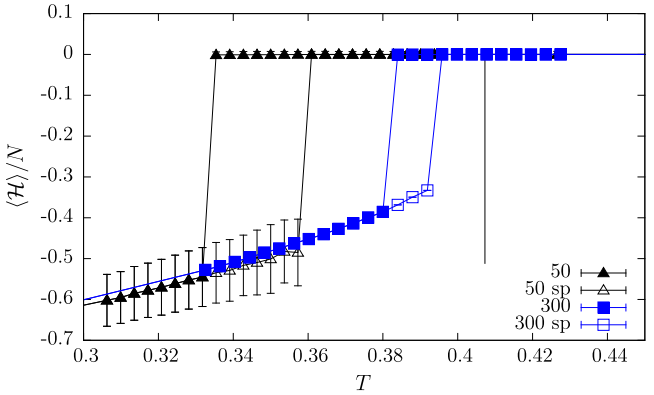

FIG. 7. (Color online) Stable and metastable energy per spin in systems with $N = 50, 300$, HTs, and with $N_4 = N^2$. The temperature end point of metastability approaches the finite-size critical temperature for large and larger sizes. The vertical line signals the mean-field critical point.

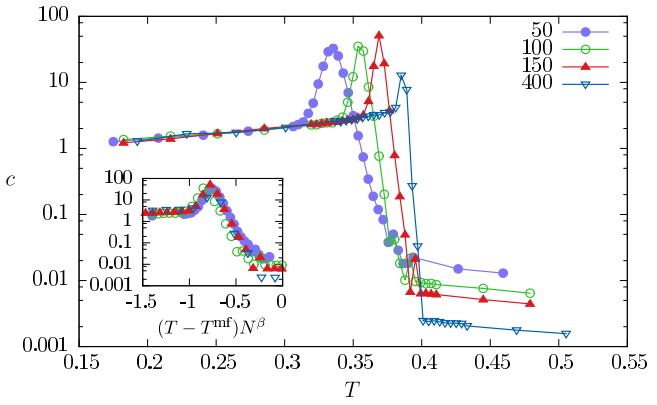

FIG. 8. (Color online) Specific heat versus temperature for different sizes of HT. The dataset is the same as Fig. 5. The inset shows the data with the scaling relation $T_c(N) - T_c^{\rm mf} \sim N^{-b}$, with $b = 0.6$.

predicts $T_s = 1/2$ in the thermodynamic limit [the metastable energy being that of Eq. (19), continued to $T_s = 1/2$]. The shrinking of the metastable interval persists even using a MC protocol which favors the relaxation towards the (low-T) metastable phase, i.e., starting from an ordered configuration and switching off the parallel tempering algorithm. The observed decreasing of the metastable interval with system size is so strong that, with the actual statistics and temperature grid, for the largest simulated sizes we are not able to observe any spinodal point distinct from the critical point in the statistical error. For the largest sizes the low-energy peak in the energy distribution associated with the ordered phase (see Fig. 6) disappears as the zero-energy peak of the paramagnetic phase appears. This situation is different from what happens in the marginal mean-field solution described in Appendix A . We note also that the finite-size nature of metastability in temperature-driven transitions has already been observed in a ferromagnetic model with pairwise interactions [45].

The specific heat is presented in Fig. 8. One observes no divergence with increasing system size, and a finite-size scaling confirming the one of the energy reported in Fig. 5. The average modulus and the magnetization are presented in Fig. 9. For high temperature, the average modulus achieves

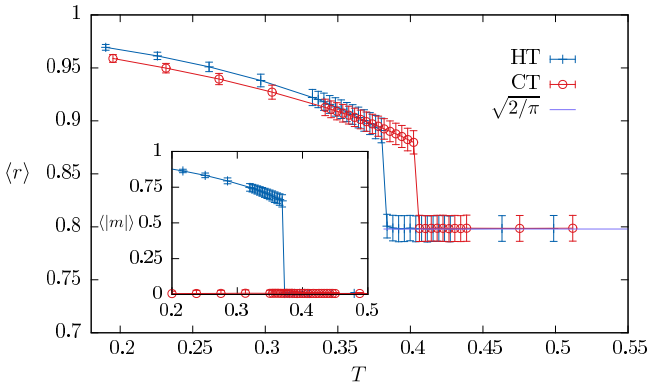

FIG. 9. (Color online) Average moduli versus temperature for systems with $N = 300$, HT, and CT. (Inset) Average modulus of the magnetization versus temperature for the two systems. The CT system is unmagnetized also at low temperatures.

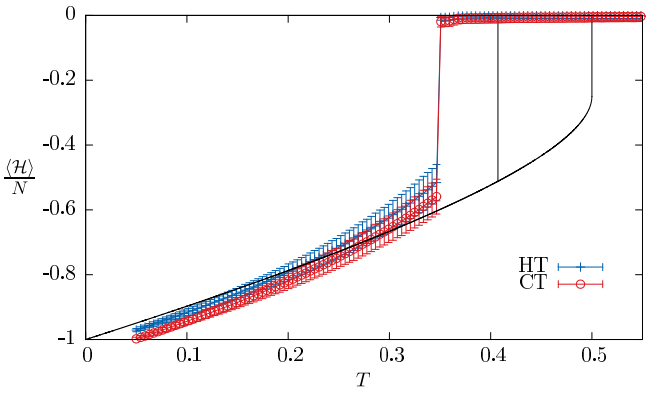

FIG. 10. (Color online) Comparison between energy of systems with HT and CT with $N = 100$ modes and $N_4 = N^2$. The black line is the marginal stable mean-field solution. The HT data are observed to converge at -1 for $T \to 0$ increasing the size, while the CT curve remains lower than the HT curve at low temperatures and converges to a value lower than one for $T \to 0$.

[up to $\mathcal{O}(N^{-1/2})$ fluctuations] the value $(2/\pi)^{1/2}$, which is the average modulus of uncorrelated complex random variables satisfying the spherical constraint, as can be exactly proven for large N. The value of $\langle r \rangle$ is discontinuous at the transition and converges to 1 for $T \to 0$, which means that all the spins exhibit equal modulus, $|a_j| = 1$. The magnetization vanishes in the high-T phase and it is 1 for zero temperature, indicating that it is of ferromagnetic nature: Not only are the moduli locked but also all the phases coincide and both phases and moduli lock at the same temperature, as predicted by mean-field theory [18].

B. Correlated topology of quadruplets

We now describe the differences induced by quadruplet correlations due to the FMC. The correlations promote fluctuations on the radial and angular degrees of freedom, not describable in mean-field approximation. As a consequence, the behavior substantially differs from that in the HT case.

1. *Absence of spontaneous O(2) symmetry breaking*

Although the transition remains first order and qualitatively equal to that of the HT case, the energy density stays below that of the HT case (see Fig. 10). Again, the energy density is independent from N_4 up to fluctuations. The most dramatic difference induced by the CT is, however, seen in the average magnetization, which vanishes *for all temperatures*. We show the change in the magnetization behavior comparing the histogram of the magnetization components $m_x = \mathrm{Re}[m]$ (Fig. 11). In both HT and CT cases, the high-temperature phase is unmagnetized with a Gaussian distribution of m_x centered in zero. In the homogeneous case, the low-temperature phase is magnetized ($|m|^2 \to 1$ for $T \to 0$) following a phase direction ($\phi = \arg m$), which is degenerated and whose average projection in the x axis results in the peaks of $h(m_x)$. For zero temperature, the distribution coincides, indeed, with $h(m) = (2\pi)^{-1}(1 - m^2)^{-1/2}$, or the m distribution corresponding to a homogeneously distributed ϕ (cf. Fig. 11); in other words, the average magnetization is zero for HT, but this happens

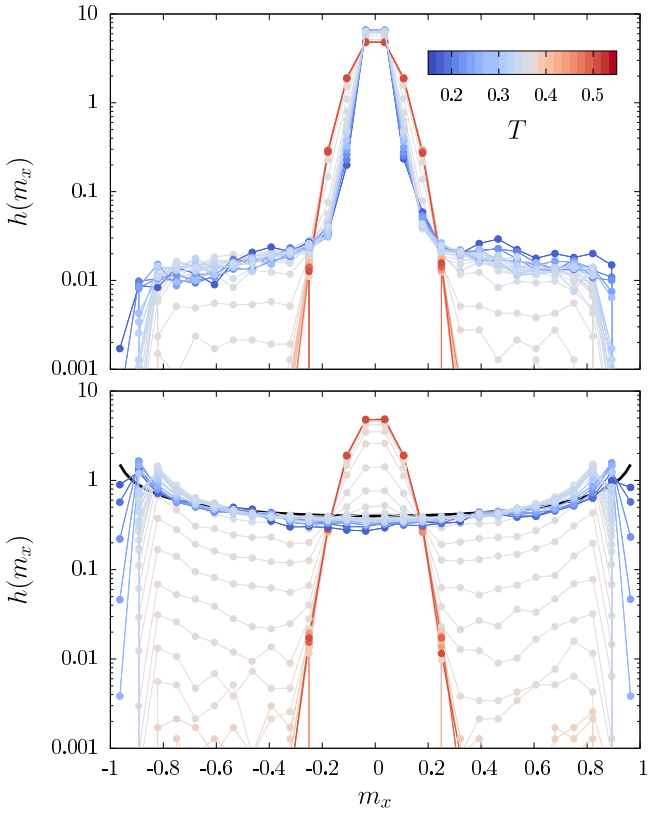

FIG. 11. (Color online) Histograms of a Cartesian component of the magnetization for two systems with $N = 300$ and $N_4 = N^2$, HT, and CT (bottom panel and top panel, respectively). The HT case is fully magnetized and for zero temperature it converges to the function $[2\pi(1-m^2)]^{-1/2}$ (indicated as a black curve in the bottom panel). The CT system is unmagnetized at all temperatures.

since the single configurations are fully magnetized over an angle which is degenerated. In the CT case, the low-temperature phase is unmagnetized instead: The average and the most probable magnetization remains zero for arbitrary low temperature, indicating an absence of global magnetic order. In the low-temperature phase, the magnetization histogram becomes nearly constant in temperature and it develops long tails.

2. *Phase wave and two-point phase correlators*

At the origin of this feature there is a property of the low-T phase with CT that we call the *phase wave* [44,46]. Modes at nearby frequencies with small value of $|i-j|$ participate in a larger number of quadruplets, since the condition Eq. (8) is more frequently satisfied than for distant modes. For this reason, nearby spins in the frequency are effectively more coupled and tend to align. This induces a phase wave [in analogy with the "spin wave" term in the context of the $O(2)$ pairwise model]: In single low-T configurations, the phases of the spins exhibit an approximated linear dependence with the frequencies ω_j [or with the spin index; see Eq. (9)], $\phi(\omega_j) \simeq \phi_0 + \Delta(\omega_j - \omega_0)$, where Δ is the phase-wave slope, a configuration-dependent quantity. In Fig. 12 we illustrate the phase wave at two different equilibrated configurations at the same temperature.

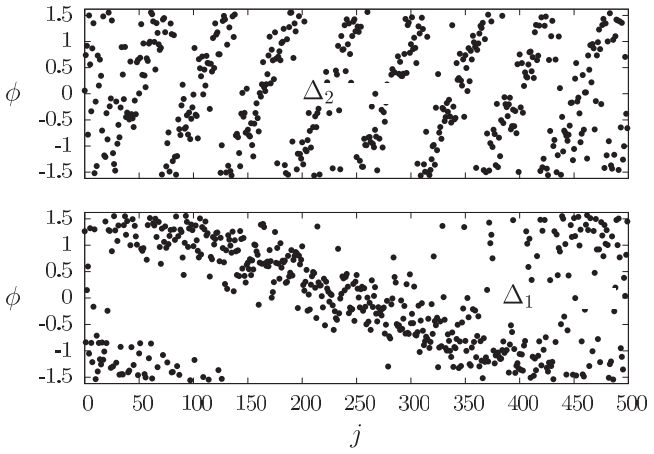

FIG. 12. Angular degree of freedom $\phi_j = \arg a_j$, versus spin index j of two single equilibrated configurations with $N = 500$ spins in a CT of quadruplets at a common undercritical temperature, $T = 0.34$. It is evident the presence of a phase wave, i.e., the approximated linear dependence of the phase on the spin index. Configurations are shown exhibiting different phase-wave slopes, Δ_1, Δ_2.

Given a realization of the quadruplet topology, there are different possible values of the phase-wave slope arising with higher probability. We consider the quantity

$$\Sigma(\Delta) = \left| \sum_{j=1}^{N} \langle \cos\phi_j \rangle \, e^{\imath 2\pi j \Delta / N} \right|. \tag{20}$$

Configurations with fixed value of the slope Δ contribute as narrow peaks of the function Σ. At a finite temperature, we observe wide peaks, as a result of thermal fluctuations, at some privileged values of Δ depending on the specific realization of the list of quadruplets (see Fig. 13), their amplitude increasing with decreasing temperature. Above the critical temperature,

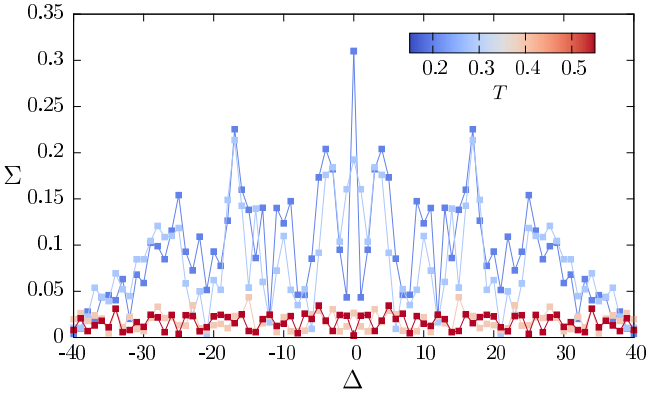

FIG. 13. (Color online) The function Σ [Eq. (20)], describing the proliferation of different phase-wave slopes, in a CT system with $N = 80$, $N_4 = N^2$, for four temperatures. The different peaks correspond to different possible slopes. At supercritical temperatures, Σ does not present peaks but uncorrelated oscillations, while at undercritical temperatures, the position of the peaks is common for all the temperatures, and the peak amplitude roughly decreases for increasing temperature.

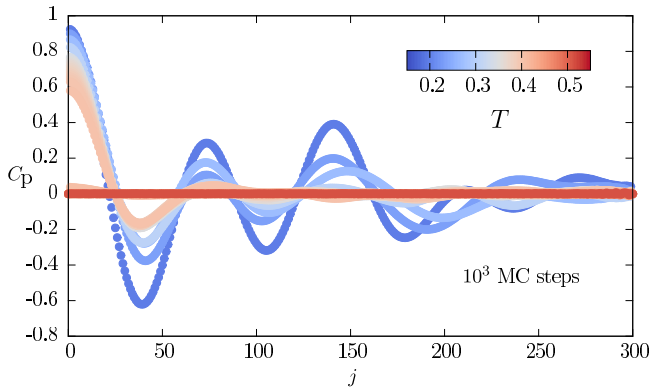

FIG. 14. (Color online) Phase-correlation function of a CT system with $N = 300$, $N_4 = N^2$, averaged over small time intervals, $\tau = 10^3$ MC steps. Different curves correspond to different temperatures. While the correlation for supercritical temperatures vanishes up to thermal fluctuations, at low temperatures it oscillates with a frequency given by the phase-wave slope.

the function Σ randomly fluctuates near zero, indicating the lack of correlation between different spins.

The phase wave is, hence, the microscopic mechanism for which there is no global $O(2)$ symmetry breaking in the low-T phase of the CT.

Phase correlation versus frequency. The phase correlation function helps to further characterize the phase wave above described. Figure 14 reports the phase correlation function C_p for a system with $N = 150$ in a CT for several temperatures. In the figure, the correlations have been *averaged over a short number ($\tau \sim 10^3$) of MC steps*. While for $T > T_c$ the phases of different spins are completely uncorrelated, the correlation is not trivial for $T < T_c$ and presents oscillations in frequency around zero, in correspondence with the phase-wave oscillations: Spins nearby in frequency (in spin index) exhibit strongly correlated orientations, at least in single configurations.

The picture, however, turns different when averaging over larger intervals of time. Our numerical results indicate that in the CT the sum of the correlations C_p over all distances decays to zero when averaged for arbitrary large MC times, at difference with the HT case (see Fig. 15 and Sec. V B 4). This gives strong evidence of the fact that the two-point angle correlators vanish even at arbitrary low temperatures. The microscopic origin of this fact is the degeneracy of phase-wave configurations with different slopes, so that phase correlations corresponding to different slopes cancel out.

3. Two-point moduli correlations

As a further insight into the low-temperature phase we present the behavior of the two-point moduli correlator. As shown in Fig. 16, the disconnected quantity C_i is approximately equal to $(2/\pi)^2$ in the high-T phase, indicating independence of moduli, while for low temperatures there is a nontrivial correlation presenting a maximum at a nonzero value of the spin frequency distance ω and decaying below the value $(2/\pi)^2$ for distant spins, which are less coupled and hence less correlated. Since spins must obey the spherical constraint, the existence of spins with moduli larger than 1 implies the

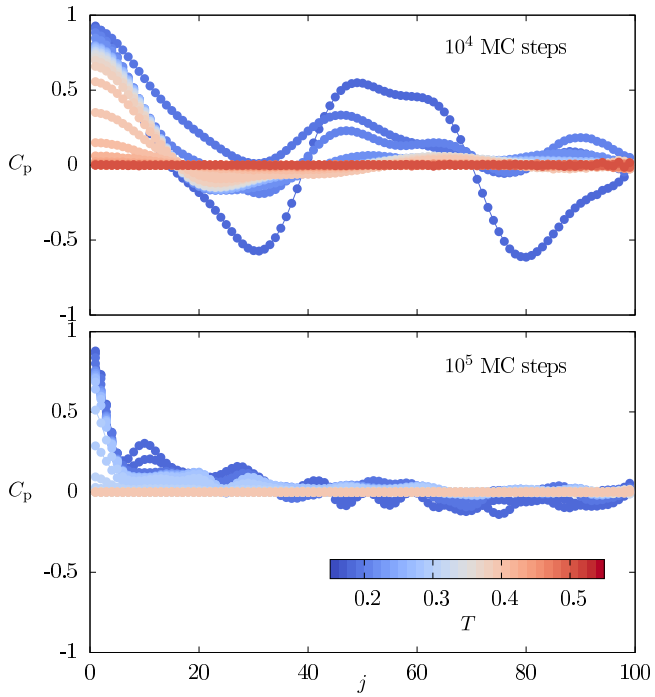

FIG. 15. (Color online) Angular two-point correlators, as in Fig. 14, but with $N = 100$ and averaged over larger intervals of local-update MC time ($\tau = 10^4$ and 10^5, top and bottom panel, respectively).

existence of other spins with moduli less than 1. However, the connected function $\tilde{C}_i$, registering the fluctuations on top of this general tendency, vanishes for large system size, as can be seen for different sizes in Fig. 16: For larger and larger sizes, the values of $\tilde{C}_i$ corresponding to both phases decrease with the value of N, along with the "gap" separating the data of both phases, which turns to be a finite-size effect of the high-temperature phase. We conclude that also moduli-moduli correlators vanish for CT in the thermodynamic limit.

4. Slow dynamics at low temperature

We now present numerical evidence of the CT system to exhibit slow dynamics at low temperatures, whose origin is the degeneracy of phase-wave configurations with different slopes. To this aim, we define *dynamical* measurements, through the *time average* $\langle\cdots\rangle_\tau = \sum_{\tau'}^{\tau}(\cdots)/\tau$ over a finite-time interval of length τ, in units of local MC steps. For sufficiently large τ, such an average coincides with the thermal average. Consequently, we define the τ-correlation function for phases and moduli, respectively, as

$$\mathcal{C}_p(\tau) = \frac{1}{N}\sum_r \Xi_\tau(r), \tag{21}$$

$$\mathcal{C}_i(\tau) = \frac{1}{N}\sum_r [\langle A_i A_j\rangle_\tau - \langle A_i\rangle_\tau\langle A_j\rangle_\tau], \tag{22}$$

$$\Xi_\tau(r) \equiv \frac{1}{N}\sum_j [\langle\cos(\phi_j - \phi_{j+r})\rangle_\tau - \langle\cos\phi_j\rangle_\tau\langle\cos\phi_{j+r}\rangle_\tau - \langle\sin\phi_j\rangle_\tau\langle\sin\phi_{j+r}\rangle_\tau], \tag{23}$$

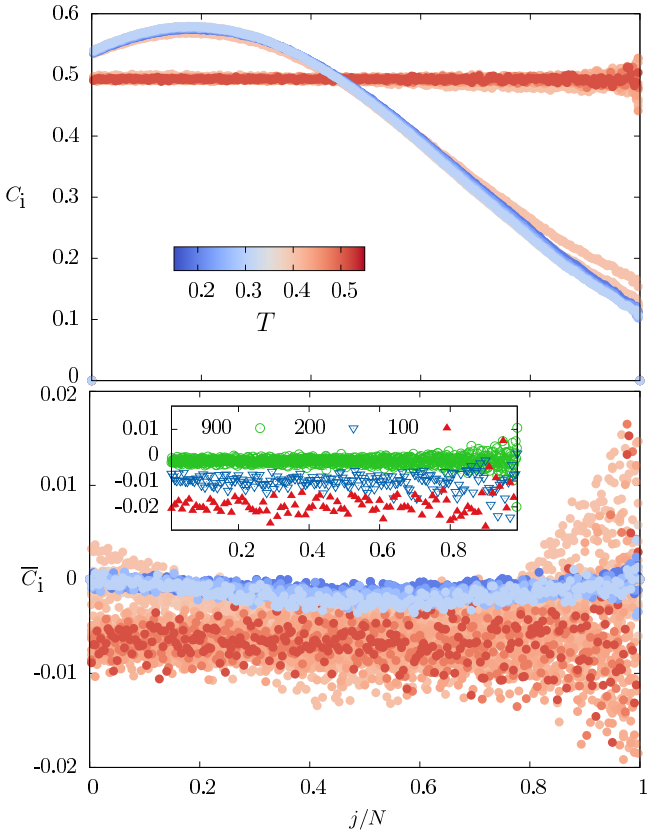

FIG. 16. (Color online) (Top) Disconnected modulus correlation function [cf., Eq. (16)], where $N = 300$, $N_4 = N^2$, and the time averages are over thermalized data in time windows of length $\tau = 10^6$. (Bottom) The connected modulus correlation function [Eq. (18)] for the same system. In the inset the connected modulus correlation function at the temperature $T = 0.46$ is shown for the sizes $N = 900, 200, 100$, showing that the function decrease for increasing sizes.

along with the *modified τ-long phase correlation function*,

$$\Psi(\tau) = \sum_{r=1}^{N} \frac{N}{K(r)} |\Xi_\tau(r)|, \tag{24}$$

where K is defined below Eq. (16). The functions $\mathcal{C}_{p,i}(\tau)$ are simply the sum of two-point correlators in different sites, while $\Psi(\tau)$ is the the sum of the absolute value of the function $\Xi_\tau(r)$ for all the possible spectral distances r. Note also that in the limit $\tau \to \infty$ the time average coincides with the equilibrium average and, thus, $\Psi(\tau \to \infty)$ is equivalent to $\sum_\omega C_p(\omega)$; cf. Eq. (17).

We stress that the function $\Psi(\tau)$ decays slower than $\mathcal{C}_p(\tau)$, and it has been defined to estimate the correlation time of the phase wave, as it does not include the anticorrelation between "distant" spins (intrinsic to the phase wave configurations) *occurring in single configurations*. Both functions, nevertheless, present a qualitatively similar behavior.

As it has been explained in the previous section, we have found strong evidence for the thermal average of both $\mathcal{C}_p$ and Ψ to vanish at low temperature in the CT and to be nonzero in the HT. Above T_c they obviously vanish for all topologies up to finite-size effects. This is illustrated in Fig. 17 for a $N = 50$

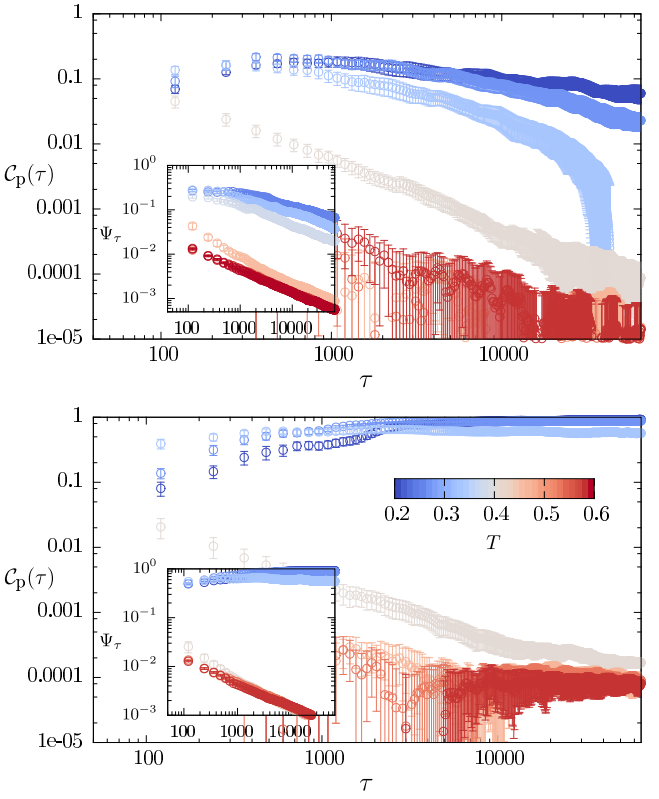

FIG. 17. (Color online) Temporal correlation functions $\mathcal{C}_p$ and Ψ for $N = 50$, $N_4 = N^2$, CT, and HTs (top and bottom panel, respectively) for several temperatures (the color code is as in Fig. 11). The finite-size critical temperature is $T(50) = 0.39(7)$.

system in the CT case, where correlations decay towards zero for sufficiently large times.

A remarkable feature of the temporal correlation functions is that, at least for CT, both $\mathcal{C}_p$ and Ψ decay slower and slower as temperature decreases. This is also reflected in the probability distribution of the phase-wave correlation time, τ_ϕ, defined as the time employed by $\Psi(\tau)$ to decay below a given threshold. Such a distribution develops long tails as temperature decreases, as shown in Ref. [44].

An explanation for such a behavior is provided by the dynamical measure of the function Σ. Its estimation in equilibrium dynamical simulations over a time window such that $\mathcal{C}_p$ in Fig. 17 has not yet decayed *presents just few peaks* or even a single peak only, corresponding to the few different phase-wave configurations with fixed slope in which the system remains trapped during a few thousand local MC steps. In this situation the use of a nonlocal update, as the parallel-tempering algorithm, is essential to thermalize the system (to get it decorrelated) in a feasible number of MC steps ($\sim 10^4$ for a system with $N = 50$), recovering the multiplicity of peaks in Fig. 13. These facts suggest a dynamical picture of the CT system according to which, at low temperatures, different phase-wave slopes are degenerated and correspond in some way to different minima in the potential energy landscape, so that the time to escape from one of them dramatically increases with decreasing T.

A careful sight suggests that a slow dynamics may be present also in the HT case, whose origin is, however, different,

being towards a nonzero value for the correlation. The analysis in the HT case is more difficult since it requires the knowledge of the thermalized probability distributions of $\mathcal{C}_{\rm p}$, Ψ at different temperatures. A deeper study is necessary to describe the dynamics of both cases in an accurate way.

The moduli temporal correlation function $\mathcal{C}_{\rm i}$ presents but quite short relaxation times even at low temperature in both HT and CT, indicating that the moduli dynamics is irrelevant in the emergence of large time scales.

VI. NUMERICAL RESULTS FOR THE *XY* MODEL

The XY model with four-body interactions [defined by the Hamiltonian Eq. (6) with quenched amplitudes, $A_j = 1$ for all j] presents as well a rich and interesting phenomenology, which we now resume.

Dense homogeneous topology. As we explained in the previous section, the moduli dynamics at low temperatures does not play any essential role in the thermodynamics of the CSM for a *dense* [$N_4 \sim \mathcal{O}(N^{\geqslant 2})$] set of quadruplets: In the low-temperature phase the moduli are more and more homogeneous and equal to 1 at lower and lower temperatures. The behavior of the $p = 4$ XY model in dense HTs, as one could expect from this argument, is indeed qualitatively identical to that of the CSM: There is a discontinuous phase transition separating a phase with uncorrelated angles and a low-T magnetized phase with $O(2)$ symmetry breaking. The finite-size critical point $T_c(N)$ is obviously higher than the CSM case (see Fig. 18). In the dilute (though dense) version, $N_4 \sim \mathcal{O}(N^2)$, we have observed how the mean-field solution [47] accurately reproduces the numerical results for energy and magnetization, with the exception of the transition temperature, which may be higher than the mean-field value (see sizes $N = 200$ and 300 in Fig. 18). In the fully connected case the critical temperature is compatible with the mean-field value.

Sparse homogeneous topology. We have also considered the case with high dilution, so that the number of quadruplets is $N_4 \sim \mathcal{O}(N^{<2})$. For the CSM, one obtains a nonequipartite condensation in such a topology, as explained in Sec. III. In the XY case, our simulations provide instead evidence that the system exhibits the mean-field behavior for $N_4 \sim \mathcal{O}(N^{>1})$. In the *homogeneously sparse* case $N_4 \sim \mathcal{O}(N)$ we observe, instead, evidence for the onset of a second-order phase transition, separating two unmagnetized phases. Remarkably, the effect of diluting until reaching sparseness has the effect of preventing the symmetry breaking. The energy presents no discontinuity while the specific heat is an increasing function of N at the transition; cf. Fig. 19. The magnetization histograms reveal an absence of angular symmetry breaking, with long tails that appear continuously at low temperatures and whose magnitude decreases with the size of the system; cf. Fig. 20. The resemblance of the *sparse* case with the unbroken symmetry in the pairwise XY model in two dimensions is discussed in the next section.

Correlated topology. Remarkably, for both $N_4 \sim \mathcal{O}(N)$ and $N_4 \sim \mathcal{O}(N^{\geqslant 2})$, our numerical analysis suggests that the phase transition remains discontinuous (differently from the HT case), with a low-temperature phase characterized by the absence of magnetization and the presence of phase waves, as in the CSM case in a dense CT. In the presence of a CT, our results indicate that the sparseness of the list of quadruplets [$N_4 \sim \mathcal{O}(N)$ in this case] *only changes the*

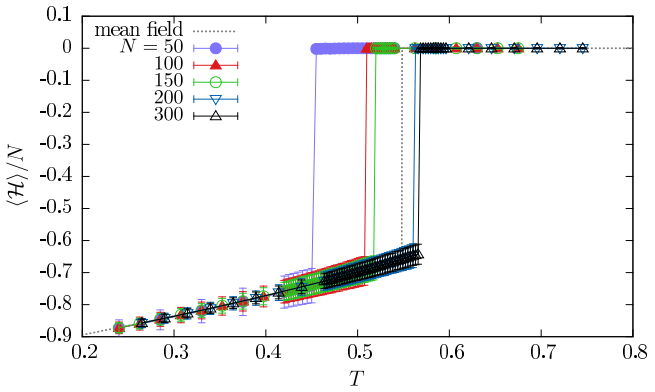

FIG. 18. (Color online) Energy of the XY model in a dense, homogeneous set of quadruplets ($N_4 = N^2$) for several sizes. The two largest have a critical transition temperature larger than the mean-field prediction. The data are indistinguishable from the mean-field result for $T < T_c^{\rm mf}$.

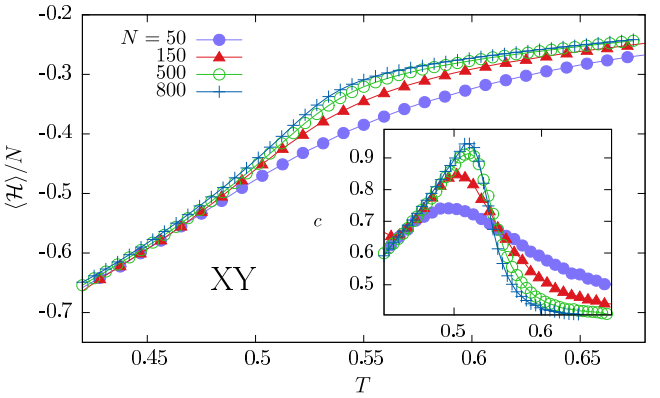

FIG. 19. (Color online) Energy of the XY model in sparse ($N_4 = N$), homogeneous sets of quadruplets for four sizes. The energy is continuous at the transition. (Inset) Specific heat for the same systems.

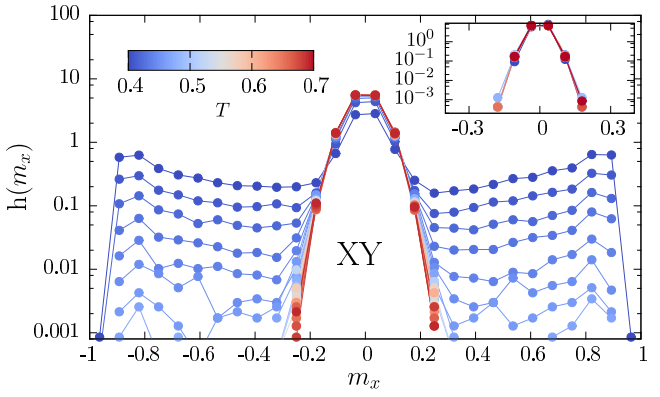

FIG. 20. (Color online) m_x histogram of the XY model in a sparse ($N_4 = N$), homogeneous set of quadruplets for $N = 150$. (Inset) m_x histogram for the size $N = 500$.

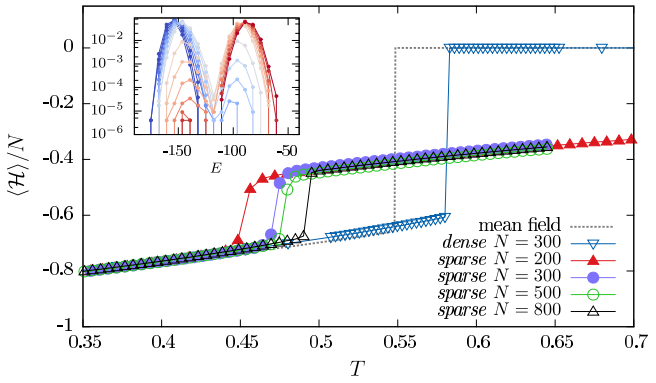

FIG. 21. (Color online) XY model energy in CTs for several sizes and two types of dilution, dense ($N_4 = N^2$) and sparse ($N_4 = N$). The inset shows the energy histogram in the sparse case with $N = 200$ and several temperatures in the range $[0.38 : 0.51]$. In the presence of CT the transition remains first order even in the sparse system, with the energy in the low-temperature phase coinciding with the mean-field theory (see main text).

high-temperature phase, which presents nonzero energy, while the transition remains first order. We present the finite-size $E(T)$ curves in Fig. 21. From our data we have concluded that the transition remains first order in the sparse case, since there is no finite-size indication of divergence in the susceptibility $\chi = N(\langle |m|^2 \rangle - |\langle m \rangle|^2)$ and since the energy histogram presents two separated peaks, with a coexistence region, as can be seen in the inset of Fig. 21. The magnetization histograms are qualitatively identical to those of the CSM in CTs in Fig. 11.

The whole picture on the type of low-temperature behavior and the symmetry conservation for all of our models happens to be rich and unexpected, and it is outlined in Table I.

A remarkable fact of the results of Fig. 21 is that the energy of the dense case coincides with the mean-field energy in the whole range $T < \min\{T_c(N), T_c^{\rm mf}\}$, although the finite-size transition temperature can be larger than the mean-field solution. Such an agreement between the CT and the HT observables (and, incidentally, between both and the mean-field theory) was absent in the CSM (see the precedent section). *The differences between the average energy on CTs and HTs are, hence, attributable to the moduli dynamics*. What is more, we observe that also in the sparse case there is an agreement between the mean-field theory and sparse and dense CT and HTs for what concerns the energy at low-enough temperatures.

VII. ANALOGY WITH THE ABELIAN LATTICE GAUGE THEORY

In the Introduction we mention the fact that the three-dimensional Abelian lattice gauge theory presents a second-order phase transition, mappable to the 2D Kosterlitz-Thouless transition. The low-temperature phase is unmagnetized, a property which follows from the model gauge invariance via Elitzur's theorem, stating that noninvariant observables under gauge transformations present a vanishing expected value in a gauge-invariant system. We believe this mechanism to be the origin of the vanishing of the magnetization also in our 4-XY model in a homogeneous sparse topology, mentioned in the previous section. According to this argument, the stochastic set of homogeneous quadruplets acquires a kind of gauge invariance. For example, it is possible that in a sparse list of random quadruplets there is a proliferation of sets of four spins occupying the bonds of four neighboring quadruplets as in Fig. 1, hence allowing for a gauge symmetry which is lost in denser topologies. This would justify the fact that in the absence of topological correlations, the one-point (magnetization) and the two-point (phase and intensity correlators) operators vanish, since they are not invariant under four-spin transformations (while four-point correlators, as the different terms in the Hamiltonian, are nonzero in general).

In any case, we stress that such a symmetry does not completely forbid the presence of magnetized configurations: In Fig. 20 one observes two maxima of the distribution $h(m_x)$ at nonzero values of m_x. These magnetizations, however, are much less probable than the most probable value at $m_x = 0$.

An analogous mechanism is behind the vanishing of the average magnetization found in both XY and spherical models in the presence of topological correlations. In this case, the transformations leaving the total energy invariant (up to fluctuations) are only those connecting phase-wave configurations with different allowed slopes (cf. Fig. 13), which are nonlocal in the sense that they involve all the spins, depending on their frequencies: $\delta\phi_i = (\Delta' - \Delta)\omega_i$. Since the magnetization and the two-point correlators are not invariant under such transformations, one expects the vanishing of their expectation values even at low temperatures.

VIII. CONNECTION WITH OPTICS AND POSSIBLE EXPERIMENTAL REALIZATIONS

Interpreted from the point of view of optics, the results of our analysis lead to several straightforward consequences in the field of multimode laser formation. Perhaps the most immediate result, not captured by approaches that neglect the role of the frequencies, is the existence of a correlated phase without global $O(2)$ order, whose microscopic origin is the phase wave. We now explain how this phase can have experimentally accessible consequences in the form of a phase delay of the ultrashort electromagnetic pulses resulting from the nontrivial mode-locking in the presence of FMC [44,46]. Such a temporal delay should be experimentally accessible, as similar carrier phase delays are measured even in ultrashort lasers [48].

A. Phase delay and phase wave

Let τ be the time measured in units of the time interval between two pulses, which in the statistical physical framework can be associated to a microscopic unit of time evolution, for example, a MC step. Let $a_n(\tau) = A_n(\tau)e^{\imath\phi_n(\tau)}$ be the nth electromagnetic mode at the MC time τ. Consider also the microscopic time unit $t \ll \tau$ describing the evolution of the electromagnetic pulse, whose form is

$$E(t|\tau) = \sum_{n=1}^{N} A_n(\tau)e^{\imath[2\pi\omega_n t + \phi_n(\tau)]}. \tag{25}$$

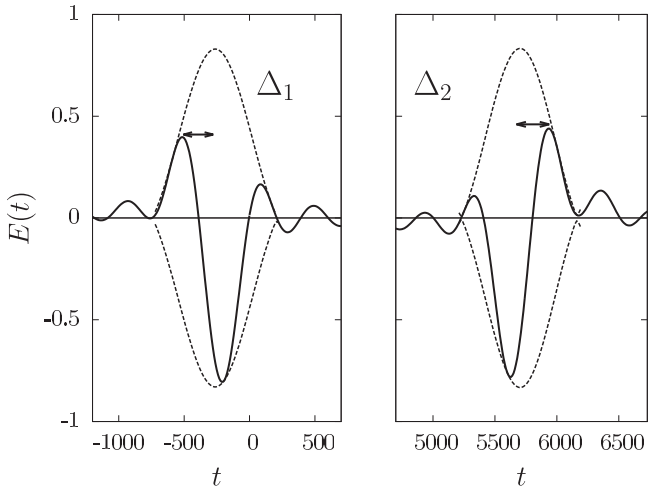

FIG. 22. Electromagnetic pulse in time [Eq. (25)], with $\omega_0 = 374$, $\delta = 1$ [cf. Eq. (9)], in correspondence of the two phase-wave configurations in Fig. 12, with slopes Δ_1 and Δ_2. The carrier-envelope delay indicated as horizontal arrows is a function of Δ and ω_0.

In the low-temperature phase (i.e., the mode-locking phase at high pumping rate) of a system with HT, all electromagnetic modes exhibit a common phase $\phi_n = \phi$ up to thermal fluctuations, and there is no phase delay in the resulting E. In contrast, the nontrivial ML induced by the CT is such that the phase velocity $dE/dt|_{t_0}$ changes from pulse to pulse, where t_0 is a reference time with respect to the position of the maximum envelope at a given τ. The time delay of the field with respect to the envelope is a nontrivial function of the phase-wave slope Δ and of the central frequency ω_0 [see Eq. (9)]. We show in Fig. 22 the form of the pulses at different thermalized configurations characterized by different τ's, and their corresponding phase waves, from which the fields E have been calculated through Eqs. (9) and (25).

In summary, the relaxation of the narrowband approximation requires the introduction of the role of mode frequencies, through the FMC, Eq. (3). We have seen in Secs. V and VI how this, in turn, induces the phase-wave mechanism. We propose that, whenever the role of the frequencies of a multimode laser is not negligible, and if the present model effectively describes the pulse formation (as is the case of the passive mode-locking laser in a closed cavity, which satisfies these two conditions), it should be observable a carrier-envelope delay of stochastic nature, of a magnitude changing, in general, from pulse to pulse (as in Fig. 22). Such single pulse dynamics, and also its relationship to experimental measurements of the average signal over several (thousands) pulses, is currently under investigation.

B. Nonequipartite condensation

The nonequipartite condensation phenomena may manifest in experimental circumstances more complicated than those of the multimode cavity resonant, such that the dilution of interaction between modes can be tuned through some mechanism. In a random laser, this is determined by the spatial separation between electromagnetic modes, since the coupling between four of them is proportional to their spatial overlap [17]. In a situation in which the leading interaction is given by the disordered version of Eq. (5), one expects to observe, by varying the spatial concentration of modes, an *abrupt transition* from a regime with single isolated peak spectra, with a few number of very intense modes, to a continuous spectra in which the optical intensity is roughly equidistributed among different modes.

In this spirit, we propose an interpretation of the results of the experiment performed in Ref. [49], the first experimental observation of the onset of mode-locking order in random lasers. In this experiment, a sample of nanoparticles is immersed in a gain medium, and the pumping protocol is such that the spatial region of the sample to be pumped can be continuously enlarged, though maintaining the overall optical power constant. In this way, when a large fraction of the sample is illuminated, the onset of a continuous collective spectra is observed, corresponding to a large amount of overlapping modes. When, instead, only part of the sample is pumped, the activated modes are low-overlapping in space, their interaction is sparse, and the intensity behavior is as that of the nonequipartite phase described in Sec. III.

C. Gain and intensity spectrum

One of the most easily accessible experimental quantities in laser setups is the intensity spectrum of the signal, $I(\omega)$. In our framework the spectra can be directly evaluated so to allow for a straightforward comparison.

For the study of the spectra, it is interesting to consider the introduction of a nonflat *gain curve* [11], which generalizes the Hamiltonian [Eq. (5)] in the following way:

$$\mathcal{H} = -\sum_s G_s A_s^2 - \frac{N}{8N_4}\sum_{spqr} \mathcal{A}_{spqr} A_s A_p A_q A_r \times \cos(\phi_s - \phi_p + \phi_q - \phi_r). \quad (26)$$

We consider Gaussian gain curves $G_s \equiv G(\omega_s)$, G being a Gaussian distribution with the maximum at the center ω_0 of the spectrum, and variance σ_g. In experiments, the temperature is typically constant, while the optical energy ϵ is ranged. To correctly compare with our simulations, where T varies at constant ϵ, we measure the intensity spectrum as $I(\omega_j) = \langle |a_j|^2 \rangle / \sqrt{T}$. In this case, to be consistent with the photonic counterpart, one also has to consider a temperature rescaled gain curve, $G(\omega, T) = T G_0(\omega)$, with a reference gain curve $G_0(\omega)$.

We now summarize the results of our numerical analysis of the Hamiltonian [Eq. (26)]. As a first observation we point out that the system behavior is robust against the inclusion of the local gain term: The critical properties and the general features of thermodynamic phases described in the previous sections remain unchanged.

In the IW regime the intensity spectrum is rather influenced by the shape of the gain curve; see Figs. 23 and 24. In general, the transition causes an abrupt change in the intensity spectrum. Above the lasing threshold, in the ML regime, the intensity spectrum is mainly determined by the topology of the interactions and it is stable against the introduction of a nonflat gain curve. For HT, the intensity spectrum is flat for high-enough pumping; see Fig. 23. This reflects the fact that in

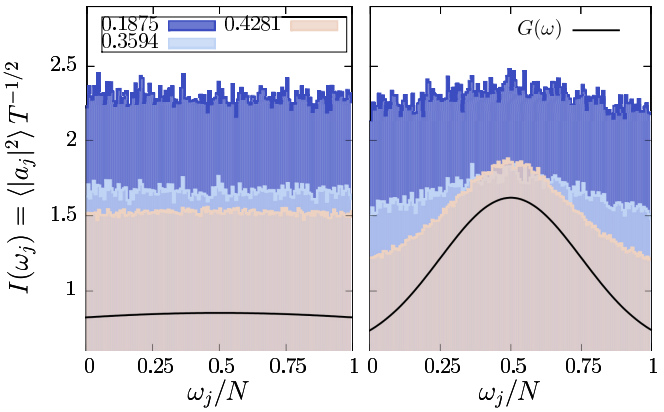

FIG. 23. (Color online) Intensity spectra for a HT system with $N = 150$ and $N_4 = N^2$ at three different temperatures. For this system the transition is at $T_c(150) = 0.369(3)$. The gain curve is Gaussian with mean in the center of the considered frequencies. (Left) Gain profile with larger variance, $\sigma_g = N$. (Right) Gain profile with smaller variance, $\sigma_g = N/4$.

HT the frequencies do not play any role, besides the gain curve, and this role becomes no longer dominant in the ML phase. In particular, comparing to the case of an approximately flat gain curve, the spectrum does not change above the transition threshold (cf. left panel of Fig. 23).

The intensity spectrum has full sense in the CT, where, instead, the frequencies play a relevant role in determining the topology. In this case, the transition is generally more abrupt in the intensity spectrum. Above the threshold the spectrum is peaked around the central frequencies disregarding the shape of the gain (Fig. 24), as the modes at the central frequencies are effectively strongly coupled (cf. Fig 2). In other words, the ML spectrum shape observed in experiments results from our analysis to be a direct consequence of the frequency-dependent mode interactions resulting from the FMC. In Fig. 25 this outcome is emphasized considering a gain curve with an average different from the central frequency of the amplified

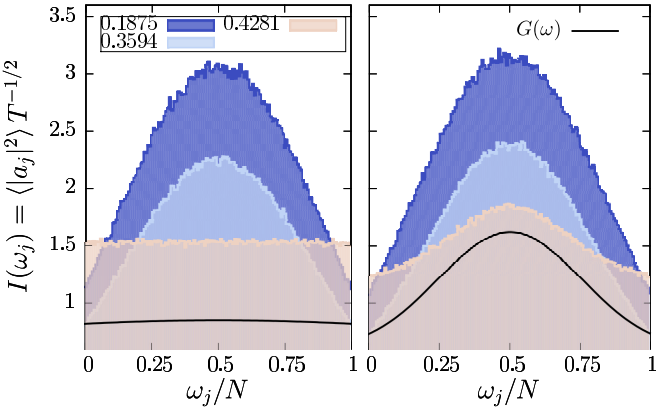

FIG. 24. (Color online) Intensity spectra for a CT system with $N = 150$ and $N_4 = N^2$ at three different temperatures. For this system the transition is at $T_c(150) = 0.386(3)$. The gain curve is Gaussian with mean in the center of the considered frequencies. (Left) Gain profile with larger variance, $\sigma_g = N$. (Right) Gain profile with smaller variance, $\sigma_g = N/4$.

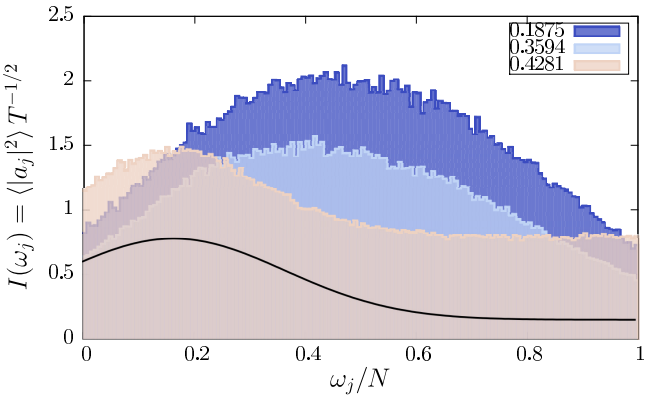

FIG. 25. (Color online) Intensity spectra for the same system of Fig. 24 but with a gain curve $\sigma_g = N/4$, centered in $\omega_j = N/6$.

spectrum: Both the frequency of maximum intensity and the whole shape of the spectrum abruptly change at the ML threshold.

The observed effect may furnish a theoretical mechanism to explain the so-called *gain-narrowing* phenomena [11,50,51].

D. Other possible experimental consequences

In this section we propose two further aspects of our analysis that may have a direct experimental consequence. The first one is the possibility of experimentally measuring the vanishing of two-point (phase and intensity) correlators. If the correlation measurements are averaged over times much larger than a light round-trip in the cavity, the vanishing of two-point correlators should be observable. The vanishing of two-point correlators may, then, signal the dominance of the nonlinear interaction mediated by the FMC, which leads to null two-point functions, as emerges from our analysis in Sec. V. Even in random lasers, intensity-intensity correlations can be measured (see, for example, Refs. [52–55]). Also, phase-phase correlations are measured in conventional lasers with standard techniques [56] and, in principle, the phase wave could be observed through phase correlation oscillations (as in Fig. 14) if a sufficiently high time resolution is achievable.

Second, according to the analysis presented in Sec. V, the metastable phase in the ML regime is expected to decrease with the size of the system. This is observed even in the HT, where the role of frequencies is irrelevant. In the optical counterpart this would imply that the region of optical bistability [57] should decrease as the number of modes in the multimode mode-locking setup increases. The other way around, the dependence/independence of this phenomena on the number of nodes could be used to infer whether the optical bistability is a consequence of the (finite-size) metastability observed in our simulations or whether its origin is different.

IX. CONCLUSIONS AND PERSPECTIVES

The present analysis studies vector statistical models with four-body interactions beyond the mean-field approximation. From our numerical study it emerges that these systems present a very rich phenomenology, among which we highlight the absence of global symmetry breaking in the presence of

quadruplet correlations, the absence of symmetry breaking and the smoothness of the transition in the XY model for $N_4 \sim \mathcal{O}(N)$ homogeneous interacting terms, the nonequipartite condensation of the complex spherical model on sparse [$N_4 \sim \mathcal{O}(N^{<2})$] graphs, and the slowing down of the dynamics in the low-temperature phase. Other rather unconventional results regarding these models are exposed in Secs. V and VI.

From a methodological point of view, we have provided a parallel algorithm to MC sample systems with $p = 4$-body interactions in an efficient way [i.e., in a time $\mathcal{O}(N_4)$ instead of $\mathcal{O}(N\,N_4)$] in the unfavorable situation in which the interaction network is nonsparse.

Moreover, we have stressed that these results, presented in a statistical physical framework, have experimental consequences in the field of photonics as these models describe also the interaction between electromagnetic modes is passive mode-locking lasers. In principle, they cover a broad range of experimental circumstances in which the modes are subject to a nonlinear quartic interaction and to a stochastic drift. In the case of laser formation the drift is induced by the spontaneous emission, considered as an effective thermal bath, and the different light regimes are associated with different resulting thermodynamic phases of the statistical model. This is well established in the case of the mode-locking transition of a closed cavity laser, which is solvable by mean-field theory in the so-called narrowband approximation [5,44]. The present work goes beyond mean field and allows to take into account frequency correlations. Our results not only account for general features of discontinuous transitions observed in mode-locking experiments, but also predicts a variety of phenomenology such as the vanishing of two-mode correlations, the carrier phase delay of electromagnetic pulses, or the nonequipartite condensation, which presumably lies at the origin of the experimental observations of Ref. [49], and in this paper we determine the conditions under which these phenomena arise. The model under analysis invites us to establish further links between the present results and other quantities measured in laser experiments, as there are further quantities provided by the MC analysis that are experimentally accessible (intensity and phase correlations and intensity spectra, hysteresis of the energy curve).

This setup allows for an analysis with additional ingredients such as quenched interaction disorder [17] and any type of interaction topology. This freedom is sufficient to enlarge the spectrum of experimental situations that may be effectively described in the statistical approach. Going beyond the passive mode-locking transition in establishing the link between optics and statistical physics is a challenging problem. That problem would include learning under what circumstances a Hamiltonian formulation is possible and what the properties of the couplings appearing in Eq. (26) describing a given experimental condition are. Such a query is indeed a big theoretical challenge, which has motivated intense research in the last years; see Ref. [20] for a review of the state of the art. In random laser phenomena there is no closed cavity and this fact poses several theoretical difficulties in the treatment, such as the very definition of lasing mode [58,59], the presence of dissipative, outer-radiative modes and their effective influence in the set of lasing modes [60], the possible existence of an imaginary part in the coupling interaction, and the existence of correlations in the coupling disorder and, possibly, in the noise [20,61].

Besides the direct photonic interpretation, the Hamiltonian Eq. (5) is quite general, and the form of topological correlations [introduced as the FMC constraint, Eq. (8)] is a very natural way of selecting the degrees of freedom which effectively interact. For this reason, we believe that the physical consequences of the present study are not limited to optics, but are possibly relevant in more general situations described by a scalar field subject to a nonlinear interaction.

ACKNOWLEDGMENTS

We thank Claudio Conti, Andrea Crisanti, Baruch Fischer, Neda Ghofraniha, Marco Leonetti, and Giorgio Parisi for motivating discussions. The research leading to these results has received funding from the Italian Ministry of Education, University and Research under the Basic Research Investigation Fund (FIRB/2008) program/CINECA Grant Code RBFR08M3P4 and under the PRIN2010 program, Grant Code 2010HXAW77-008 and from the People Programme (Marie Curie Actions) of the European Union's Seventh Framework Programme FP7/2007-2013/ under REA Grant Agreement No. 290038, NETADIS project.

APPENDIX A: THE MEAN-FIELD SOLUTION OF THE FERROMAGNETIC MODEL

Consider the fully connected ferromagnetic model

$$\mathcal{H} = -\frac{1}{N^3}\sum_{jklm}^{1,N} a_j a_k a_l^* a_m^*, \qquad \text{with} \quad \sum_j |a_j|^2 = \epsilon N. \tag{A1}$$

Defining $a_j = \sigma_j + i\tau_j$, the partition function is

$$\mathcal{Z} = \int_S \exp\left[\frac{\beta}{N^3}\sum_{jklm}(\sigma_{jklm} + \tau_{jklm} + \varphi_{jklm})\right] d\boldsymbol{\sigma}\, d\boldsymbol{\tau},$$

where the subscript $\mathcal{S}$ means that the integral is evaluated over the hypersphere [Eq. (A1)] and

$$\varphi_{1234} = \tfrac{1}{3}(\psi_{12,34} + \psi_{13,24} + \psi_{14,23}),$$
$$\psi_{12,34} = \sigma_{12}\tau_{34} + \sigma_{34}\tau_{12},$$

and we are using the shortening

$$\sigma_{12\cdots k} = \sigma_1\sigma_2\cdots\sigma_k.$$

Introducing the magnetizations

$$m_\sigma = \frac{1}{N}\sum_j \sigma_j, \quad m_\tau = \frac{1}{N}\sum_j \tau_j,$$

the partition function is written as

$$\mathcal{Z} = \int \mathcal{D}\mathbf{m}\, e^{-N\beta F(\mathbf{m})},$$

with

$$\beta F(\mathbf{m}) = -\beta\left(m_\sigma^2 + m_\tau^2\right)^2 - \ln\left[\pi\left(\epsilon - m_\sigma^2 - m_\tau^2\right)\right] - 1.$$

Solving the integral over the magnetizations with the saddle-point method leads us to consider

$$\beta\frac{dF}{dm_{\sigma,\tau}} = 2m_{\sigma,\tau}\left[-2\beta\left(m_\sigma^2+m_\tau^2\right)+\frac{1}{\epsilon-m_\sigma^2-m_\tau^2}\right]=0.$$

The paramagnetic (PM) case with $m_\sigma = m_\tau = 0$ is always a solution. For

$$\epsilon^2\beta > 1 \quad \rightarrow \quad T < \epsilon^2, \tag{A2}$$

also a ferromagnetic (FM) solution appears with

$$m_\sigma^2 + m_\tau^2 = \frac{\epsilon}{2}\left(1+\sqrt{1-\frac{1}{\epsilon^2\beta}}\right).$$

The average energy is

$$\langle\mathcal{H}\rangle = -\frac{\partial}{\partial\beta}\ln\mathcal{Z} = -\epsilon^2\left(m_\sigma^2+m_\tau^2\right)^2+\mathcal{O}\left(\frac{1}{N}\right),$$

and it is zero for the PM solution and

$$\frac{\langle\mathcal{H}\rangle}{N} = -\frac{\epsilon^4}{4}\left(1+\sqrt{1-\frac{1}{\epsilon^2\beta}}\right)^2 \tag{A3}$$

for the FM solution.

The Hessian of the functional F yields the stability properties of the previous solutions. The PM solution $m_\sigma = m_\tau = 0$ is associated with two degenerate positive eigenvalues, so the PM solution is always stable. The FM solution has a *null eigenvalue* and a positive eigenvalues; then, in the region where the FM solution exists, it is always marginally stable.

Then, in the region of the phase diagram given by Eq. (A2), the stable PM and the marginal FM solutions coexist. The equilibrium transition is at the point

$$\epsilon^2\beta_c = 2.455\,408\ldots,$$

where the free energy of the two solutions are equal. At lower temperature $F_{\rm fm} < F_{\rm pm}$ and the PM solution becomes metastable.

APPENDIX B: ENERGY SCALING IN THE DISORDERED SPHERICAL MODEL

We suppose a Gaussian distribution of couplings $P(J)$, with average J_0 and variance σ. In this case, we can write an n-replicated partition function,

$$\begin{aligned}\overline{\mathcal{Z}^n} &= \int\prod_{j=1}^N da_j da_j^* \int\prod_{[jklm]} J^{(4)}_{[jklm]}P(J_{[jklm]})\exp\left\{-\beta\sum_{b=1}^n\mathcal{H}_J[\{a^{(b)}\}]\right\}\\ &= \sqrt{2\pi\sigma^2}\int\prod_{j=1}^N da_j da_j^*\exp\left\{\sum_{[jklm]}^{1,N}\left[J_0\beta\sum_{b=1}^n a_j^b a_k^{b*}a_l^b a_m^{b,*}+\frac{1}{2}\sigma^2\beta^2\left(\sum_b a_j^b a_k^{b,*}a_l^b a_m^{b,*}\right)^2\right]\right\},\end{aligned}$$

where $[jklm]$ points out distinct interacting quadruplets. Unlike the fully connected case, in a diluted case the "spatial" index of the modes is not removed. However, just for scaling purposes, one can try and use a mean-field approximation for the diluted case as well, assuming that $\sum_{N_4}\sim(N_4/N^4)\sum_{jklm}$, where the sum runs over all indices. In this way one can rewrite the exponent in terms of the overlap matrices and magnetizations as usual, so to obtain (cf. Ref. [18])

$$\begin{aligned}\frac{E}{N} &= -\frac{1}{N}\frac{d}{d\beta}\overline{\ln\mathcal{Z}} = -\frac{1}{N}\frac{d}{d\beta}\lim_{n\to0}\frac{\overline{\mathcal{Z}^n}-1}{n}\\ &= -\frac{1}{2}\sum_b g(Q_{b1},R_{b1})-k(m_\sigma,m_\tau),\end{aligned}$$

where ($a_1\equiv\sigma_1+i\tau_1$)

$$\begin{aligned}Q_{ab} &= \sum_1\frac{\sigma_1^a\sigma_1^b+\tau_1^a\tau_1^b}{2N},\\ R_{ab} &= \sum_1\frac{\sigma_1^a\sigma_1^b-\tau_1^a\tau_1^b}{2N},\quad m_\sigma=\frac{1}{N}\sum_1\sigma_1,\\ g(Q_{ab},R_{ab}) &= \beta\left(Q_{ab}^2+R_{ab}^2\right)\left[\frac{1}{9}\sigma_4^2\left(Q_{ab}^2+R_{ab}^2\right)\frac{N_4}{N}\right],\\ k\left(m_\sigma^a,m_\tau^a\right) &= \frac{1}{2}\left[\left(m_\sigma^a\right)^2+\left(m_\tau^a\right)^2\right]\left\{\frac{1}{12}J_0^{(4)}\left[\left(m_\sigma^a\right)^2+\left(m_\tau^a\right)^2\right]\frac{N_4}{N}\right\}.\end{aligned}$$

In the case of equipartition, one has $\mathcal{O}(N)$ spins of amplitude $\mathcal{O}(1)$, so all the overlap matrices and magnetizations are $\mathcal{O}(1)$. Then the extensive energy in both cases results as in Eq. (12).

[1] A. Fratalocchi, C. Conti, G. Ruocco, and S. Trillo, Phys. Rev. Lett. **101**, 044101 (2008).
[2] G. A. El and A. M. Kamchatnov, Phys. Rev. Lett. **95**, 204101 (2005).
[3] K. O. Rasmussen, T. Cretegny, P. G. Kevrekidis, and N. Grønbech-Jensen, Phys. Rev. Lett. **84**, 3740 (2000).
[4] J. A. Krumhansl and J. R. Schrieffer, Phys. Rev. B **11**, 3535 (1975).
[5] A. Gordon and B. Fischer, Phys. Rev. Lett. **89**, 103901 (2002).
[6] A. Gordon and B. Fischer, Optics Commun. **223**, 151 (2003).
[7] B. Vodonos, R. Weill, A. Gordon, A. Bekker, V. Smulakovsky, O. Gat, and B. Fischer, Phys. Rev. Lett. **93**, 153901 (2004).
[8] A. Gordon and B. Fischer, Opt. Lett. **29**, 1022 (2004).
[9] M. Katz, A. Gordon, O. Gat, and B. Fischer, Phys. Rev. Lett. **97**, 113902 (2006).
[10] A. Picozzi, J. Garnier, T. Hansson, P. Suret, S. Randoux, G. Millot, and D. Christodoulides, Phys. Rep. **542**, 1 (2014).
[11] H. Haus, IEEE J. Sel. Top. Quantum Electron. **6**, 1173 (2000).
[12] C. Van den Broeck, J. M. R. Parrondo, and R. Toral, Phys. Rev. Lett. **73**, 3395 (1994).
[13] R. W. Boyd, *Nonlinear Optics*, 3rd ed. (Academic Press, San Diego, 2008).
[14] R. Weill, A. Rosen, A. Gordon, O. Gat, and B. Fischer, Phys. Rev. Lett. **95**, 013903 (2005).
[15] L. Angelani, C. Conti, G. Ruocco, and F. Zamponi, Phys. Rev. Lett. **96**, 065702 (2006).
[16] L. Leuzzi, C. Conti, V. Folli, L. Angelani, and G. Ruocco, Phys. Rev. Lett. **102**, 083901 (2009).
[17] C. Conti and L. Leuzzi, Phys. Rev. B **83**, 134204 (2011).
[18] F. Antenucci, C. Conti, A. Crisanti, and L. Leuzzi, Phys. Rev. Lett. **114**, 043901 (2015).
[19] D. S. Wiersma, Nat. Phys. **4**, 359 (2008).
[20] F. Antenucci, A. Crisanti, and L. Leuzzi, Phys. Rev. A **91**, 053816 (2015).
[21] E. Fermi, J. Pasta, and S. Ulam, Lect. Appl. Math. **15**, 143 (1974).
[22] C.-J. Chen, P. K. A. Wai, and C. R. Menyuk, Opt. Lett. **19**, 198 (1994).
[23] J. B. Kogut, Rev. Mod. Phys. **51**, 659 (1979).
[24] J. E. Moore and D.-H. Lee, Phys. Rev. B **69**, 104511 (2004).
[25] C. Xu and J. E. Moore, Phys. Rev. Lett. **93**, 047003 (2004).
[26] O. G. Mouritsen, B. Frank, and D. Mukamel, Phys. Rev. B **27**, 3018 (1983).
[27] J.P. Bouchaud and M. Mézard, J. Phys. I **4**, 1109 (1994).
[28] A. Lipowski, J. Phys. A: Math. Gen. **30**, 7365 (1997).
[29] A. Lipowski and D. Johnston, Phys. Rev. E **61**, 6375 (2000).
[30] A. Lipowski, D. Johnston, and D. Espriu, Phys. Rev. E **62**, 3404 (2000).
[31] A. Lipowski and D. Johnston, J. Phys. A: Math. Gen. **33**, 4451 (2000).
[32] Y. Nishiyama, Phys. Rev. E **70**, 026120 (2004).
[33] R. L. Jack, J. P. Garrahan, and D. Sherrington, Phys. Rev. E **71**, 036112 (2005).
[34] R. Ambartzumian, G. Savvidy, K. Savvidy, and G. Sukiasian, Phys. Lett. B **275**, 99 (1992).
[35] G. Savvidy and K. Savvidy, Phys. Lett. B **337**, 333 (1994).
[36] D. Espriu, M. Baig, D. A. Johnston, and R. P. K. C. Malmini, J. Phys. A: Math. Gen. **30**, 405 (1997).
[37] M. R. Swift, H. Bokil, R. D. M. Travasso, and A. J. Bray, Phys. Rev. B **62**, 11494 (2000).
[38] P. Dimopoulos, D. Espriu, E. Jané, and A. Prats, Phys. Rev. E **66**, 056112 (2002).
[39] C. Castelnovo, C. Chamon, and D. Sherrington, Phys. Rev. B **81**, 184303 (2010).
[40] Bernasconi, J., J. Phys. (Paris) **48**, 559 (1987).
[41] E. Marinari, G. Parisi, and F. Ritort, J. Phys. A: Math. Gen. **27**, 7615 (1994).
[42] M. I. Berganza and L. Leuzzi, Phys. Rev. B **88**, 144104 (2013).
[43] F. D. Nobre and A. A. Júnior, Phys. Lett. A **288**, 271 (2001).
[44] F. Antenucci, M. I. Berganza, and L. Leuzzi, Phys. Rev. A **91**, 043811 (2015).
[45] M. Ibáñez Berganza, P. Coletti, and A. Petri, Europhys. Lett. **106**, 56001 (2014).
[46] A. Marruzzo and L. Leuzzi, Phys. Rev. B **91**, 054201 (2015).
[47] L. Angelani, C. Conti, L. Prignano, G. Ruocco, and F. Zamponi, Phys. Rev. B **76**, 064202 (2007).
[48] T. Brabec and F. Krausz, Rev. Mod. Phys. **72**, 545 (2000).
[49] M. Leonetti, C. Conti, and C. Lopez, Nat. Photon. **5**, 615 (2011).
[50] M. Horowitz, R. Daisy, B. Fischer, and J. Zyskind, Electron. Lett. **30**, 648 (1994).
[51] M. Horowitz, R. Daisy, B. Fischer, and J. L. Zyskind, Opt. Lett. **19**, 1406 (1994).
[52] N. Ghofraniha, I. Viola, F. Di Maria, G. Barbarella, G. Gigli, L. Leuzzi, and C. Conti, Nat. Commun. **6** (2015).
[53] M. Leonetti, C. Conti, and C. López, Phys. Rev. A **88**, 043834 (2013).
[54] X. Wu and H. Cao, Opt. Lett. **32**, 3089 (2007).
[55] S. Mujumdar, V. Türck, R. Torre, and D. S. Wiersma, Phys. Rev. A **76**, 033807 (2007).
[56] R. Trebino, *Frequency-Resolved Optical Gating: The Measurement of Ultrashort Laser Pulses: The Measurement of Ultrashort Laser Pulses* (Springer, Berlin, 2000), Vol. 1.
[57] H. Gibbs, *Optical Bistability: Controlling Light with Light* (Elsevier, Amsterdam, 1985).
[58] S. M. Dutra and G. Nienhuis, Phys. Rev. A **62**, 063805 (2000).
[59] H. E. Türeci, A. D. Stone, and B. Collier, Phys. Rev. A **74**, 043822 (2006).
[60] C. Viviescas and G. Hackenbroich, Phys. Rev. A **67**, 013805 (2003).
[61] G. Hackenbroich, C. Viviescas, and F. Haake, Phys. Rev. A **68**, 063805 (2003).